Received: 4 September 2018 | Revised: 19 August 2019 | Accepted: 26 August 2019
DOI: 10.1002/fld.4767

RESEARCH ARTICLE

WILEY

A technique of flux reconstruction at the interfaces of nonconforming grids for aeroacoustic simulations

Sophie Le Bras[1,2] | **Hugues Deniau**[3] | **Christophe Bogey**[4]

[1]Centre Européen de Recherche et de Formation Avancée en Calcul Scientifique, , Toulouse, France

[2]Siemens Industry Software N.V., Leuven, Belgium

[3]ONERA, French Aerospace Lab, Toulouse, France

[4]Univ Lyon, Ecole Centrale de Lyon, INSA Lyon, Université Claude Bernard Lyon I, CNRS, Laboratoire de Mécanique des Fluides et d'Acoustique, UMR 5509, Ecully, France

Correspondence
Sophie Le Bras, Siemens Industry Software N.V., Interleuvenlaan 68, 3001 Leuven, Belgium.
Email: sophie.le_bras@siemens.com

Summary

A flux reconstruction technique is presented to perform aeroacoustic computations using implicit high-order spatial schemes on multiblock structured grids with nonconforming interfaces. The use of such grids, with mesh spacing discontinuities across the block interfaces, eases local mesh refinements, simplifies the mesh generation process, and thus facilitates the computation of turbulent flows. In this work, the spatial discretization consists of sixth-order finite-volume implicit schemes with low-dispersion and low-dissipation properties. The flux reconstruction is based on the combination of noncentered schemes with local interpolations to define ghost cells and compute flux values at the grid interfaces. The flow variables in the ghost cells are calculated from the flow field in the grid cells using a meshless interpolation with radial basis functions. In this study, the flux reconstruction is applied to both plane and curved nonconforming interfaces. The performance of the method is first evaluated by performing two-dimensional simulations of the propagation of an acoustic pulse and of the convection of a vortex on Cartesian and wavy grids. No significant spurious noise is produced at the grid interfaces. The applicability of the flux reconstruction to a three-dimensional computation is then demonstrated by simulating a jet at a Mach number of 0.9 and a diameter-based Reynolds number of 4×10^5 on a Cartesian grid. The nonconforming grid interface located downstream of the jet potential core does not appreciably affect the flow development and the jet sound field, while reducing the number of mesh points by a factor of approximately two.

KEYWORDS

aeroacoustics, finite volumes, high-order schemes, meshless interpolation, nonconforming grids, structured grids

1 | INTRODUCTION

For flows at high Reynolds numbers, the direct computation of the aerodynamic noise from the Navier-Stokes equations requires accurate numerical methods to properly compute both the small turbulent motions and the low-frequency sound waves in the radiated pressure field.[1-3] To meet these requirements, in addition to high-order discretization schemes, locally refined meshes are needed to capture the turbulent eddies generating noise.[4]

For aeroacoustic simulations performed on multiblock structured grids, the computational domain is usually divided into subdomains composed of conforming grids characterized by a full point-matching distribution at the block interface,

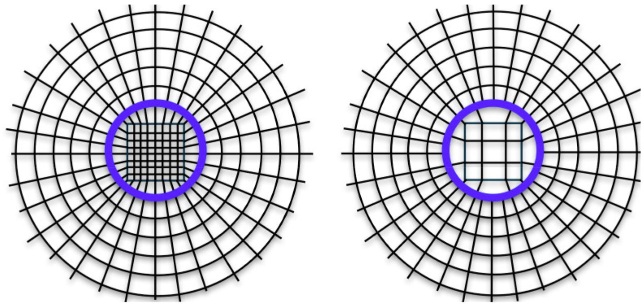

FIGURE 1 Representation of two-dimensional meshes with (A) conforming and (B) nonconforming grid interfaces in blue [Colour figure can be viewed at wileyonlinelibrary.com]

as shown in Figure 1A. Difficulties in performing high-fidelity computations with such grids arise when the geometries are complex. Such geometries must be included in the numerical simulations to faithfully reproduce the conditions of the experiments.[5,6] In this context, high-quality structured meshes with conforming interfaces are in many cases almost impossible to generate.[7] For instance, for high-speed flows exhausting from turbofan jet engines or developing on aircraft wings,[8] extremely fine grids are required to resolve the flow in the boundary layers and the wakes. Using conforming grids, local mesh refinements can be found in all the computational domains, leading to an excessive number of mesh points as well as to the generation of extremely small cells in out of interest areas. Obviously, this increases the computational cost of the simulation. In addition, using an explicit time discretization scheme, the presence of very small mesh cells imposes severe constraints on the time step so that the Courant-Friedrichs-Lewy (CFL) restriction is verified.[3]

To perform aeroacoustic simulations of high-Reynolds-number flows at a reasonable computational cost, the use of nonconforming grids[9] without overlapping is attractive. Such meshes exhibit discontinuities of the grid lines across the block interface. This is the case of Figure 1B, providing an example of a nonconforming mesh with discontinuous grid spacings in the azimuthal direction at the block interface in blue. Using such a mesh for instance, the refinement at the center of the grid in Figure 1A can be avoided. The size of the smallest cells and thus the time step are therefore chosen such that the acoustic sources are well discretized. In addition, the use of nonconforming grids simplifies the grid generation process since the mesh blocks composing the computational domain can be created independently and then easily assembled. In return, to obtain high-fidelity numerical results using nonconforming grids, an accurate spatial discretization at the grid interfaces is required. Indeed, as the grid spacing is discontinuous at the block interface, the spatial discretization schemes cannot usually be applied close to the interface and their formulations have to be modified.

In computational aeroacoustics, the spatial discretization can be carried out using high-order low-dissipation and low-dispersion schemes, among which the dispersion-relation-preserving schemes,[10] the optimized explicit schemes in the Fourier space,[2] or the implicit schemes.[11,12] In this study, the spatial discretization consists of the sixth-order finite-volume implicit scheme of Pouangué et al[12] in combination with the sixth-order implicit selective filter of Visbal and Gaitonde.[13] Implicit schemes are particularly attractive to reach a high-order spectral accuracy using a smaller number of grid points compared with explicit schemes. However, in the context of parallel computations, the flow equations are generally solved locally in each subdomain of the multiblock grid. As a consequence, the implicit centered schemes cannot be applied at the mesh block interfaces. Therefore, in a previous study,[12] a technique of flux reconstruction at the interface of conforming grids has been developed. Based on the application of noncentered spatial schemes at the block interface and the use of ghost cells, the technique allowed us to successfully perform massively parallel aerodynamic and aeroacoustic computations of jet flows.[14-17]

In the present study, a flux reconstruction technique for the interface of nonconforming grids is proposed. The technique, derived from the method developed for conforming grids,[12] is based on the application of noncentered schemes at the grid interface. Due to the mesh line discontinuities at the grid interface, an additional step consisting in reconstructing ghost cells is required. The flow variables in the ghost cells are computed using a local interpolation technique, based on a meshless method involving radial basis functions (RBFs).[9,18] Meshless interpolations are useful in alleviating the difficulties caused by the loss of the mesh topology at the interfaces of nonconforming grids. Indeed, since meshless interpolations are performed from arbitrarily scattered spatial data without any geometrical information, computational overheads due to topology reconstructions are avoided. Originally developed by Le Bras et al for plane nonconforming grid interfaces,[19] the technique of flux reconstruction is extended to curved interfaces in this study. In comparison with the preliminary results presented by Le Bras et al,[19] the properties of the RBF interpolation are examined in one dimension (1-D) in the wavenumber space, and the performance of the flux reconstruction is further assessed by simulating in two dimensions (2-D) the convection of a vortex on wavy grids and the propagation of an acoustic pulse. In addition, the application of the technique to a three-dimensional (3-D) turbulent jet flow is presented.

The present paper is organized as follows. In Section 2, the high-order finite-volume approach used in this study, and the flux reconstruction method for conforming interfaces are described. In Section 3, the reconstruction technique developed at the interface of plane and curved nonconforming grids is presented. In Section 4, the properties of the RBF interpolations are examined in 1-D in the wavenumber space. In Section 5, the accuracy of the flux reconstruction is evaluated by simulating a 2-D acoustic pulse propagating through a nonconforming interface. In Section 6, the simulations of 2-D vortex convection for Cartesian and wavy grids with different spatial resolutions are presented. In particular, the advantages of using RBF interpolations for the reconstruction and the choice of the interpolation parameters are discussed. Finally, the application of the technique to a 3-D turbulent jet flow is presented, using a nonconforming grid downstream of the jet potential core. The reduction in the number of mesh points obtained using a nonconforming grid is evaluated. The effects of the presence of a nonconforming interface on the sound field radiated by the jet are examined.

2 | FLUX RECONSTRUCTION TECHNIQUE FOR CONFORMING GRIDS

2.1 | Governing equations

In this study, the 3-D compressible Navier-Stokes equations are solved. Using Cartesian coordinates, they can be written as

$$\frac{\partial \mathbf{W}}{\partial t} + \frac{\partial \mathbf{E}_c}{\partial x} + \frac{\partial \mathbf{F}_c}{\partial y} + \frac{\partial \mathbf{G}_c}{\partial z} - \frac{\partial \mathbf{E}_d}{\partial x} - \frac{\partial \mathbf{F}_d}{\partial y} - \frac{\partial \mathbf{G}_d}{\partial z} = 0, \tag{1}$$

where ($\mathbf{E}_c$, $\mathbf{F}_c$, and $\mathbf{G}_c$) are the convective fluxes; ($\mathbf{E}_d$, $\mathbf{F}_d$, and $\mathbf{G}_d$) are the diffusive fluxes; $\mathbf{W} = (\rho, \rho u, \rho v, \rho w, \rho e)^t$ is the vector of the conservative variables; ρ is the density; (u, v, w) are the velocity components; and ρe is the total energy. For a perfect gas, the total energy ρe is given by

$$\rho e = \frac{p}{\gamma - 1} + \frac{1}{2}\rho(u^2 + v^2 + w^2), \tag{2}$$

where p is the static pressure and γ is the specific heat ratio. The convective fluxes write as

$$\begin{cases} \mathbf{E}_c = (\rho u, \rho u^2 + p, \rho uv, \rho uw, (\rho e + p)u)^t \\ \mathbf{F}_c = (\rho v, \rho uv, \rho v^2 + p, \rho vw, (\rho e + p)v)^t \\ \mathbf{G}_c = (\rho w, \rho uw, \rho vw, \rho w^2 + p, (\rho e + p)w)^t \end{cases} \tag{3}$$

and the diffusive fluxes as

$$\begin{cases} \mathbf{E}_d = (0, \tau_{11}, \tau_{12}, \tau_{13}, \tau_{11}u + \tau_{12}v + \tau_{13}w + H_1)^t \\ \mathbf{F}_d = (0, \tau_{21}, \tau_{22}, \tau_{23}, \tau_{21}u + \tau_{22}v + \tau_{23}w + H_2)^t \\ \mathbf{G}_d = (0, \tau_{31}, \tau_{32}, \tau_{33}, \tau_{31}u + \tau_{32}v + \tau_{33}w + H_3)^t \end{cases} \tag{4}$$

where $\mathbf{H} = (H_1, H_2, H_3)^t$ is the heat flux vector, $\tau_{ij} = 2\mu S_{ij}$ is the viscous stress tensor, μ is the dynamic molecular viscosity computed from Sutherland's law, and S_{ij} is the deformation stress tensor:

$$S_{ij} = \frac{1}{2}\left(\frac{\partial u_i}{\partial x_j} + \frac{\partial u_j}{\partial x_i} - \frac{2}{3}\frac{\partial u_k}{\partial x_k}\delta_{i,j}\right). \tag{5}$$

The heat flux vector $\mathbf{H}$ is computed from Fourier's law, yielding

$$\mathbf{H} = -\lambda \nabla T, \tag{6}$$

where ∇T is the temperature gradient, $\lambda = C_p\mu/Pr$ is the thermal conductivity, C_p is the specific heat at constant pressure, and Pr is the Prandtl number.

2.2 | High-order finite-volume approach

The computations are performed using the finite-volume multiblock structured solver ***elsA***,[20] allowing us to perform direct numerical simulations or large-eddy simulations (LES). In a finite-volume approach, the integral form of the Navier-Stokes equation (1) is solved at a discrete level. For this purpose, the computational domain is divided into nonoverlapping control volumes Ω_i, where i is the volume index. Integrating Equation (1) over the elementary volumes Ω_i and using the divergence theorem lead to

$$|\Omega_i|\frac{d\mathbf{U}_i}{dt} + \int_{\partial\Omega_i} (\mathbf{E}_c + \mathbf{F}_c + \mathbf{G}_c)\cdot \boldsymbol{n}\ \mathrm{d}S + \int_{\partial\Omega_i} (\mathbf{E}_d + \mathbf{F}_d + \mathbf{G}_d)\cdot \boldsymbol{n}\ \mathrm{d}S = 0, \tag{7}$$

where $\boldsymbol{n} = (n_x, n_y, n_z)$ is the outgoing unitary normal of Ω_i, $\partial\Omega_i$ represents the faces of Ω_i, and $\mathbf{U}_i$ is the mean value of $\mathbf{W}$ in the volume Ω_i such as

$$\mathbf{U}_i = \frac{1}{|\Omega_i|}\int_{\Omega_i} \mathbf{W}\,\mathrm{d}V. \tag{8}$$

In the ***elsA*** solver, the diffusive fluxes in Equation (7) are calculated from the gradient $\nabla\mathbf{U}$ estimated at the cell interfaces using a second-order method.[21] For clarity, in the following, only the convective fluxes are presented in the equations. Following Pouangué et al.[12] and supposing that the volume Ω_i is an hexahedron, the normal $\boldsymbol{n}$ is constant along the interface, and the integral of the convective fluxes in Equation (7) can be approximated as

$$\int_{\partial\Omega_i} (\mathbf{E}_c + \mathbf{F}_c + \mathbf{G}_c)\cdot \boldsymbol{n}\,\mathrm{d}S \simeq |\partial\Omega_i| \left(\mathbf{E}_c(\widetilde{\mathbf{U}}_{\partial\Omega_i})n_x + \mathbf{F}_c(\widetilde{\mathbf{U}}_{\partial\Omega_i})n_y + \mathbf{G}_c(\widetilde{\mathbf{U}}_{\partial\Omega_i})n_z\right), \tag{9}$$

where $\widetilde{\mathbf{U}}_{\partial\Omega_i}$ is the averaged value of the variable vector $\mathbf{W}$ at the cell interface $\partial\Omega_i$:

$$\widetilde{\mathbf{U}}_{\partial\Omega_i} = \frac{1}{|\partial\Omega_i|}\int_{\partial\Omega_i} \mathbf{W}\,\mathrm{d}S. \tag{10}$$

The convective fluxes are thus computed from the interface-averaged values $\widetilde{\mathbf{U}}$ of the flow variables. To obtain a high-order calculation of the convective fluxes derivatives, a high-order interpolation of vector $\widetilde{\mathbf{U}}$ is performed from the cell-averaged values $\mathbf{U}$. Considering the 1-D computational domain of Figure 2, the interpolated vector $\widetilde{\mathbf{U}}$ at the interface $i + 1/2$ is obtained by solving the implicit scheme:

$$\alpha_{i+1/2}\widetilde{\mathbf{U}}_{i-1/2} + \widetilde{\mathbf{U}}_{i+1/2} + \beta_{i+1/2}\widetilde{\mathbf{U}}_{i+3/2} = \sum_{l=-1}^{2} a_l \mathbf{U}_{i+l}, \tag{11}$$

where $\alpha_{i+1/2}$, $\beta_{i+1/2}$, and a_l are the scheme coefficients that are obtained from a fifth-order Taylor series.[12] This scheme correctly resolves the wavelengths discretized by at least five points.[14] Note that despite the use of approximation (9), which is formally only second-order accurate, Pouangué et al.[12] demonstrated that the numerical scheme (11) is equivalent to Lele's sixth-order finite-difference scheme[11] for a uniform Cartesian mesh.

To ensure the stability of the centered scheme (11), the sixth-order compact filter of Visbal and Gaitonde[13] is applied to the flow variables. The filtered values, denoted $\widehat{\mathbf{U}}$, are estimated from the values of $\mathbf{U}$ as

$$\alpha_f\widehat{\mathbf{U}}_{i-1} + \widehat{\mathbf{U}}_i + \alpha_f\widehat{\mathbf{U}}_{i+1} = \sum_{l=0}^{3}\frac{\gamma_l}{2}\left(\mathbf{U}_{i+l} + \mathbf{U}_{i-l}\right), \tag{12}$$

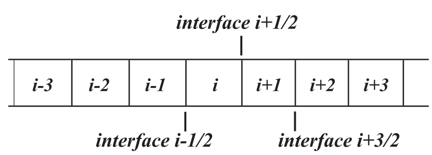

FIGURE 2 Representation of a one-dimensional computational domain

where $\alpha_f = 0.47$ and γ_l are the filter coefficients.[13] The filter is employed on a uniformly spaced grid due to a coordinate transform. For LES computations, the filter also plays the role of a subgrid-scale model, relaxing turbulent energy at high frequencies.[22-24] Time integration is performed by applying a low-storage six-stage Runge-Kutta algorithm.[2] Radiation boundary conditions, Navier-Stokes characteristic boundary conditions, and sponge zones are used to avoid significant acoustic reflections at the mesh boundaries. A more detailed description of the numerical algorithm is given by Pouangué et al.[14]

2.3 | Reconstruction for conforming grid interfaces

2.3.1 | Numerical scheme

At the mesh-block interfaces, the implicit centered scheme (11) used in the computation of the convective fluxes cannot be applied. Thus, in a previous study,[12] a flux reconstruction technique has been proposed at the interfaces of conforming grids. It is presented in the following by considering a 2-D computational domain composed of two blocks L and R separated by a conforming interface, as shown in Figure 3.

The reconstruction technique consists of two steps. In the first step, the flow variables $\widetilde{\mathbf{U}}$ at the grid interface in blocks L and R are determined using upwind schemes. More precisely, in block L, as illustrated in Figure 3A, the vector $\widetilde{\mathbf{U}}_L$ at the interface I_L is computed using a noncentered scheme involving the flow variables in cells of blocks L and R such as

$$\alpha' \widetilde{\mathbf{U}}_{i=N-1/2,j} + \widetilde{\mathbf{U}}_L = \underbrace{a'_0 \mathbf{U}_{i=N-1,j} + a'_1 \mathbf{U}_{i=N,j}}_{\text{cells of block L}} + \underbrace{a'_2 \mathbf{U}_{i'=0,j} + a'_3 \mathbf{U}_{i'=1,j}}_{\text{cells of block R}}, \tag{13}$$

where α' and a'_i are the scheme coefficients determined using Taylor series. For block L, the values of $\mathbf{U}$ in the cells $(i' = 0, j)$ and $(i' = 1, j)$ of block R are a priori not known. These cells are thus referred to as ghost cells for block L in the following. The values of $\mathbf{U}$ in the ghost cells are obtained due to data exchanges between the blocks at each time iteration of the simulation. Symmetrically, in block R, the vector $\widetilde{\mathbf{U}}_R$ at the interface I_R in Figure 3B is determined from the upwind scheme:

$$\widetilde{\mathbf{U}}_R + \beta'' \widetilde{\mathbf{U}}_{i'=1/2,j} = \underbrace{a''_0 \mathbf{U}_{i=N-1,j} + a''_1 \mathbf{U}_{i=N,j}}_{\text{cells of block L}} + \underbrace{a''_2 \mathbf{U}_{i'=0,j} + a''_3 \mathbf{U}_{i'=1,j}}_{\text{cells of block R}} \tag{14}$$

where β'' and a''_i are the scheme coefficients. The values of $\widetilde{\mathbf{U}}_L$ and $\widetilde{\mathbf{U}}_R$ are usually not identical, since they are determined from two different upwind schemes (13) and (14). Therefore, in a second step, a Riemann problem[25] is solved to ensure the unicity of the flux, hence the scheme conservativity, at the block interface.

2.3.2 | Selective filter

In the vicinity of conforming grid interfaces, as for the centered scheme (11), the seven-point centered filter (12) cannot be applied, and its formulation has to be modified. However, previous studies[26] demonstrated that the change of the filter formulation at the grid interface is likely to significantly decrease the accuracy of the filtering process and generate spurious noise. Therefore, to still apply the centered filter (12) at the grid interface, Pouangué[26] proposed to artificially extend the size of the mesh blocks using ghost cells, and to modify the filter formulation in the ghost cell regions exclusively. In practice, according to the notations of Figure 4, in order to change the filter formulation as far as possible from the interface, the block L is extended using five ghost cells represented by stars. These cells correspond to the cells of block R indexed by $i' = 0, 1, 2, 3, 4$. Consequently, in block L, the centered filter (12) on seven points can be applied in cells

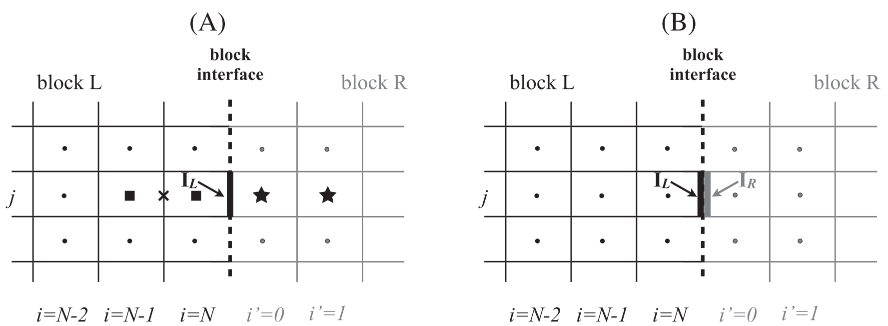

FIGURE 3 Flux reconstruction for conforming grids: (A) Step 1: computation of the flow variables at the interface I_L using a scheme involving two cells (squares) and an interface (cross) of block L and two ghost cells (stars) of block R, and (B) step 2: flux computation from the flow variables at the interfaces I_L and I_R, using a Riemann solver

$i = \dots, N-1, N$ and in the ghost cell $(i' = 0, j)$. Finally, a noncentered filter is used to determine the value of $\widehat{\mathbf{U}}$ in the ghost cell $(i' = 1, j)$ in gray in Figure 4:

$$\alpha_f \widehat{\mathbf{U}}_{i'=0,j} + \widehat{\mathbf{U}}_{i'=1,j} = \sum_{k=2}^{3} \frac{\gamma_k}{2} \mathbf{U}_{i=N-k+2,j} + \frac{\gamma_1}{2} \mathbf{U}_{i'=0,j} + \gamma_0 \mathbf{U}_{i'=1,j} + \sum_{k=1}^{3} \frac{\gamma_k}{2} \mathbf{U}_{i'=k+1,j} - \alpha_f \mathbf{U}_{i'=2,j}. \tag{15}$$

The flux reconstruction for conforming grids presented in this section has been successfully applied to massively parallel aeroacoustic simulations of jet flows at high Reynolds numbers.[14,15,17]

3 | FLUX RECONSTRUCTION TECHNIQUE FOR NONCONFORMING GRIDS

In this section, the reconstruction presented above for conforming grids is extended to the cases of plane and curved nonconforming meshes.

3.1 | Plane interfaces

In the case of a nonconforming grid interface, as illustrated in Figure 5, the flux reconstruction technique described in Section 2.3 cannot be used. Indeed, for such grids, as the mesh lines are discontinuous across the block interface, the ghost cells represented by stars in Figure 4 are no longer defined. Therefore, the upwind schemes (13) and (14) and the filter (15) cannot be applied. In this work, a new flux reconstruction is thus proposed at the nonconforming interfaces. It consists in using noncentered schemes and meshless interpolations to define the flow variables in ghost cells and at the grid interface. In this section, the flux reconstruction is presented for the plane grid interface displayed in Figure 5, considering block L as the current block.

3.1.1 | Numerical scheme

To compute the flux at the interface I_L in block L, the key idea is to make possible the application of the schemes (13) and (14) due to the reconstruction of the flow variables in ghost cells. For this purpose, a methodology, composed of four steps depicted in Figure 5, is presented. In step 1, two ghost cells, represented in gray in Figure 5A, are defined. The centers of these cells, depicted by stars, are located at the intersection between the mesh lines $i' = 0$ and $i' = 1$ and the straight line passing by the centers of the cells $(i = N-1, j)$ and $(i = N, j)$. The values of the flow variables $\mathbf{U}$ in the ghost cells are determined from the values of $\mathbf{U}$ in the cells of block R using a meshless interpolation. The interpolation technique is presented in Section 3.1.3. In Step 2, illustrated in Figure 5B, the upwind scheme (13) can be applied to compute the flow vector $\widetilde{\mathbf{U}}_L$ at the interface I_L of block L. In step 3, symmetrically with what was done in steps 1 and 2 for block L, ghost cells are defined in block R, and the scheme (14) is employed to determine the vector $\widetilde{\mathbf{U}}$ at the interfaces $(\dots, I_{R,j'}, I_{R,j'+1}, \dots)$ in gray in Figure 5C. Finally, in step 4, a ghost interface I'_L, identical geometrically to I_L, is defined in block R, as shown in Figure 5D. The variable vector $\widetilde{\mathbf{U}}'_L$ at the interface I'_L is interpolated from the values $\widetilde{\mathbf{U}}$ obtained in step 3. This second interpolation method is also described in Section 3.1.3. Even if the interfaces I'_L and I_L are geometrically identical, the values of $\widetilde{\mathbf{U}}$ at these two interfaces differ since they are computed from different schemes and interpolations. Therefore, the convective flux at the block interface is determined from the values of $\widetilde{\mathbf{U}}_L$ and $\widetilde{\mathbf{U}}'_L$ by resolving a Riemann flux problem.[25]

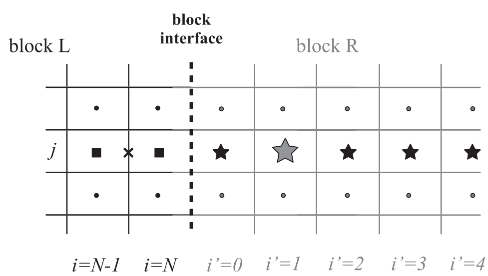

FIGURE 4 Filter application in block L in the vicinity of a conforming grid interface: The flow variables in the ghost cell $i' = 1$ in gray are filtered using grid cells of block L (squares) and block R (stars)

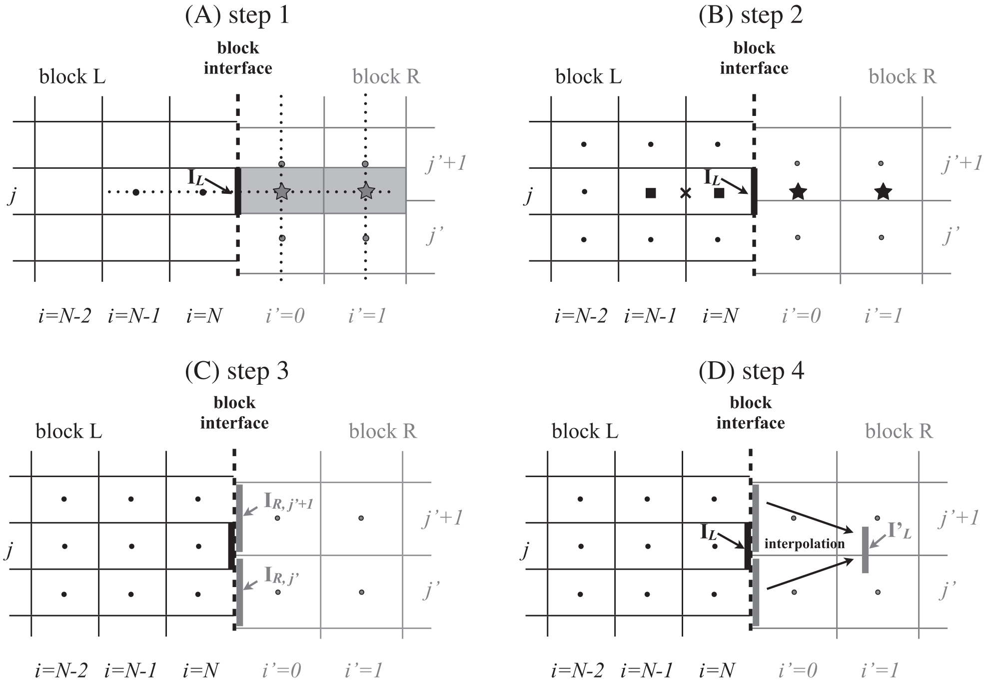

FIGURE 5 Flux reconstruction for nonconforming grids at the interface I_L in block L: (A) Step 1: Definition of two ghost cells (stars); (B) Step 2: Computation of the flow variables at the interface I_L using a noncentered scheme involving an interface (cross) and two cells (squares) of block L, and two ghost cells (stars); (C) Step 3: Computation of the flow variables at the interfaces in gray, applying steps 1 and 2 in block R; and (D) Step 4: Interpolation of the flow variables at the ghost interface I'_L using the data computed in step 3, and computation of the resulting flux at the block interface using a Riemann solver

3.1.2 | Selective filter

Five ghost cells are necessary to apply the noncentered filter (15) near the block interface. For conforming grids, as explained in Section 2.3, the flow variables in the ghost cells are directly obtained due to data exchanges between blocks. However, for nonconforming grids, these variables first need to be interpolated before being exchanged. Consequently, using five ghost cells results in an extra computational cost compared with conforming grids, which led us to only consider two ghost cells. The application of the filter close to the nonconforming interface of block L is illustrated in Figure 6. The cells and ghost cells of block L involved in the filtering are represented by squares and stars, respectively. As shown in Figure 6A, using two ghost cells, the seven-point centered filter (12) can be applied as far as point $(i = N-1, j)$ in block L. At the cell $(i = N, j)$ adjacent to the block interface, in gray in Figure 6B, the filtered field $\widehat{\mathbf{U}}_{i=N,j}$ is computed from the upwind formulation:

$$\alpha_f \widehat{\mathbf{U}}_{i=N-1,j} + \widehat{\mathbf{U}}_{i=N,j} + \alpha_f \widehat{\mathbf{U}}_{i'=0,j} = \sum_{k=0}^{4} \gamma'_k \mathbf{U}_{N-4+k,j} + \gamma'_5 \mathbf{U}_{i'=0,j} + \gamma'_6 \mathbf{U}_{i'=1,j}. \tag{16}$$

Finally, the flow variables in the ghost cells $(i' = 0, j)$ and $(i' = 1, j)$ are filtered using noncentered schemes on seven points, as illustrated in Figures 6C and 6D, yielding

$$\begin{cases} \alpha_f \widehat{\mathbf{U}}_{i=N,j} + \widehat{\mathbf{U}}_{i'=0,j} + \alpha_f \widehat{\mathbf{U}}_{i'=1,j} & = \displaystyle\sum_{k=0}^{4} \gamma''_k \mathbf{U}_{N-4+k,j} + \gamma''_5 \mathbf{U}_{i'=0,j} + \gamma''_6 \mathbf{U}_{i'=1,j} \\ \alpha_f \widehat{\mathbf{U}}_{i'=0,j} + \widehat{\mathbf{U}}_{i'=1,j} & = \displaystyle\sum_{k=0}^{4} \gamma'''_k \mathbf{U}_{N-4+k,j} + \gamma'''_5 \mathbf{U}_{i'=0,j} + \gamma'''_6 \mathbf{U}_{i'=1,j}, \end{cases} \tag{17}$$

where $\alpha_f = 0.47$ and γ'_k, γ''_k, and γ'''_k are the noncentered filter coefficients.[27]

3.1.3 | Interpolation techniques

In the flux reconstruction for nonconforming grids, interpolations are performed to compute the flow variables $\mathbf{U}$ in two ghost cells and the values of $\widetilde{\mathbf{U}}$ at the grid interface. As presented in Section 3.1.1, in block L, the interpolations are carried out using values of $\mathbf{U}$ and $\widetilde{\mathbf{U}}$ in block R. In practice, block R can be divided into subdomains with a loss of topology information between the domains. Therefore, in this study, meshless interpolations based on RBFs are employed.

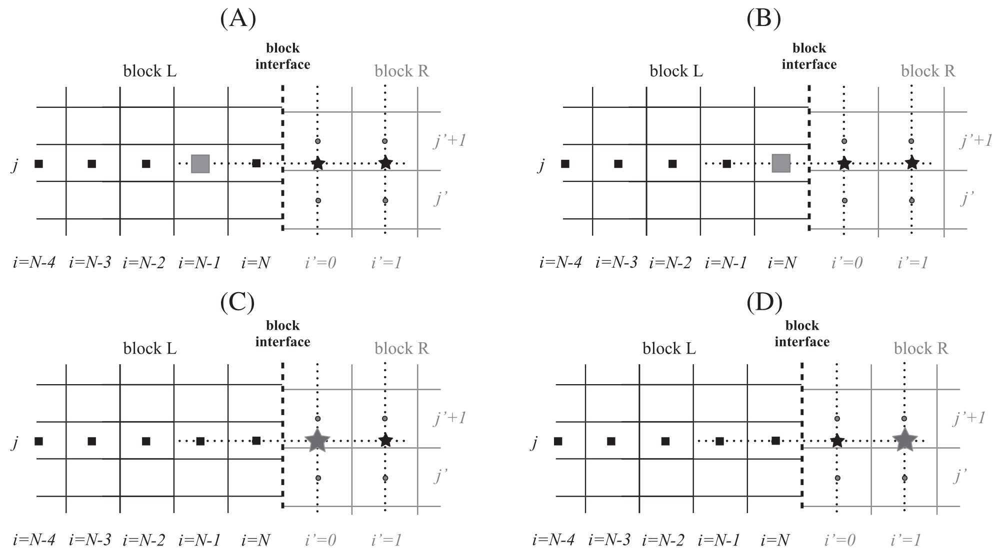

FIGURE 6 Filtering at the nonconforming grid interface in block L. Cells in block L (squares) and ghost cells in block R (stars) used in the filter scheme applied at points: (A) $(i = N-1, j)$, (B) $(i = N, j)$, (C) $(i' = 0, j)$, and (D) $(i' = 1, j)$

First, the interpolation technique is described for the calculation of a component u of the vector $\mathbf{U}$ in the ghost cell located at $i' = 0$ in Figure 5A. The calculation is performed using the value of u known in n_v cells of block R surrounding the ghost cell. These n_v cells are located along the line $i' = 0$ for a 2-D mesh, in the plane $i' = 0$ for a 3-D straight mesh. The RBF approximation u_{RBF} of the variable u at point $\boldsymbol{x}$ writes[9]

$$u_{\mathrm{RBF}}(\boldsymbol{x}) = \sum_{j=1}^{n_v} \xi_j \Phi(\boldsymbol{x}, \boldsymbol{x}_j) + \sum_{q=1}^{m} \zeta_q P_q(\boldsymbol{x}), \tag{18}$$

where ξ_j and ζ_q are the unknown interpolation coefficients, $(\boldsymbol{x}_j)_{j=1,\ldots,n_v}$ are the centers of the n_v cells, Φ are Wendland's RBFs,[9,28] and $\sum \zeta_q P_q(\boldsymbol{x}) = \zeta_0 + \zeta_1 x + \zeta_2 y + \ldots + \zeta_m z^{\deg(\mathrm{P})}$ is a polynomial term of degree deg(P) that ensures the unicity of the approximation u_{RBF}.[18,29] The calculation of the coefficients ξ_j and ζ_q is presented in Appendix A.1. Similarly, the value of $\mathbf{U}$ in the second ghost cell in Figure 5A is interpolated using the RBF approximation (18) and n_v points located at $i' = 1$. The choice of the interpolation parameters n_v and deg(P) in Equation (18) is discussed in Sections 6 and 7.

A second interpolation technique is proposed to interpolate the flow variables $\widetilde{\mathbf{U}}$ at the block interface I'_L in Figure 5D. As for the interpolation of the flow field in the ghost cells, an RBF interpolation is carried out. However, the quantity to interpolate is not a single-point value u but an averaged value $\tilde{u}$ on a grid interface. Therefore, the interpolation of $\tilde{u}$ on the interface I'_L is performed from n_v values of $\widetilde{\mathbf{U}}$ at the interfaces $(I_{R,1}, \ldots, I_{R,j'}, I_{R,j'+1}, \ldots, I_{R,n_v})$ represented in gray in Figure 5C. The interpolation formulation at the grid interface I'_L is obtained by integrating Equation (18) on I'_L:

$$\begin{aligned} \tilde{u}_{L'} &= \frac{1}{|I'_L|} \int_{I'_L} u_{\mathrm{RBF}}(\boldsymbol{x}) \mathrm{d}\boldsymbol{x} \\ &= \sum_{j'=1}^{n_v} \tilde{\xi}_{j'} \left(\frac{1}{|I'_L|} \int_{I'_L} \Phi(\boldsymbol{x}, \boldsymbol{x}_{j'}) \mathrm{d}\boldsymbol{x} \right) + \sum_{q=1}^{m} \tilde{\zeta}_q \left(\frac{1}{|I'_L|} \int_{I'_L} P_q(\boldsymbol{x}) \mathrm{d}\boldsymbol{x} \right), \end{aligned} \tag{19}$$

where the point $\boldsymbol{x}_{j'}$ is the center of the surface $I_{R,j'}$. The calculation of the interpolation coefficients $\tilde{\xi}_{j'}$ and $\tilde{\zeta}_q$ is detailed in Appendix A.2.1. A third-order Gaussian quadrature is used to compute the integrals of Equation (19). In practice, the interpolation coefficients in Equations (18) and (19) are computed only once at the beginning of the simulation and stored in memory, yielding low CPU cost interpolations (see Appendix A).

3.2 | Curved interfaces

For curved grid interfaces, the flux reconstruction presented in Section 3.1 cannot be applied. For the interpolation of the flow variables at the grid interface using Equation (19), as the curvature of the surface is not taken into account to define the ghost interface I'_L, the integral (19) is evaluated on a plane interface that does match the shape of the nonconforming interface. Therefore, a flux reconstruction for curved nonconforming interfaces is also proposed. The objective is to find a function $\sigma(\boldsymbol{x})$ to define a curved interface $I'_{L_{\text{curved}}}$ knowing only the position $\boldsymbol{x}$ of the mesh points. The flow variables at the interface $I'_{L_{\text{curved}}}$ are then calculated as in Equation (19):

$$\begin{aligned}\tilde{u}_{L'} &= \frac{1}{\left|I'_{L_{\text{curved}}}\right|}\int_{I'_{L_{\text{curved}}}} u_{\text{RBF}}(\boldsymbol{x})\mathrm{d}\boldsymbol{x} \\ &= \sum_{j'=1}^{n_v}\widetilde{\xi}_{j'}\left(\frac{1}{\left|I'_{L_{\text{curved}}}\right|}\int_{I'_{L_{\text{curved}}}}\Phi(\boldsymbol{x},\boldsymbol{x}_{j'})\mathrm{d}\boldsymbol{x}\right)+\sum_{q=1}^{m}\widetilde{\zeta}_q\left(\frac{1}{\left|I'_{L_{\text{curved}}}\right|}\int_{I'_{L_{\text{curved}}}}P_q(\boldsymbol{x})\mathrm{d}\boldsymbol{x}\right)\end{aligned} \tag{20}$$

The calculation of the RBF coefficients $\widetilde{\xi}_{j'}$ and $\widetilde{\zeta}_q$ is described in Appendix A.2.2.

The method to determine the function σ is presented for the 2-D grid of Figure 7A, composed of two blocks L and R separated by a curved interface. The curved interfaces to be defined by the function σ are denoted by $I'_{L_{\text{curved}}}$ and $(I_{R,1_{\text{curved}}},\dots,I_{R,j'_{\text{curved}}},I_{R,j'+1_{\text{curved}}},\dots,I_{R,n_{v_{\text{curved}}}})$. To determine the function σ, a technique proposed by Carr et al.[30] for 3-D imaging reconstruction is employed. First, relations to be verified by the function σ at given mesh points are imposed. In particular, at the N_p grid points of blocks L and R lying on the interfaces $(I_{R,1_{\text{curved}}},\dots,I_{R,j'_{\text{curved}}},I_{R,j'+1_{\text{curved}}},\dots,I_{R,n_{v_{\text{curved}}}})$ in Figure 7A, the function σ cancels out:

$$\sigma(\boldsymbol{x}_i)=0 \quad \text{for} \quad 1\le i\le N_p, \tag{21}$$

where $\boldsymbol{x}_i = (x_i, y_i, z_i)$ are the spatial coordinates of the ith mesh point. To ensure that function σ differs from the zero-function, off-surface points are considered and nonzero values are given to the function σ at these points. In the present study, n_v points of block L and n_v points of block R are selected, corresponding to the centers of the cells adjacent to the grid interface. They are represented by black and gray circles in Figure 7B for $n_v = 3$. A value of $\sigma = -1$ is given to the n_v points of block L, and $\sigma = 1$ is attributed to the n_v points of block R. Thus, the objective is to find the function σ so that the following relations are satisfied:

$$\begin{cases}\sigma(\boldsymbol{x}_i)=0 & \text{for} \quad 1\le i\le N_p\\ \sigma(\boldsymbol{x}_r)=1 & \text{for} \quad 1\le r\le n_v\\ \sigma(\boldsymbol{x}_l)=-1 & \text{for} \quad 1\le l\le n_v\end{cases} \tag{22}$$

where $(\boldsymbol{x}_r)_{1,\dots,n_v}$ and $(\boldsymbol{x}_l)_{1,\dots,n_v}$ are the positions of the centers of the n_v cells of blocks L and R, respectively. Then, given the set of points $S_N = [(\boldsymbol{x}_i)_{1,\dots,N_p},(\boldsymbol{x}_r)_{1,\dots,n_v},(\boldsymbol{x}_l)_{1,\dots,n_v}] = [(\boldsymbol{x}_j)_{1,\dots,N_S}]$ and the relations (22), the function σ is calculated by RBF interpolation[30]:

$$\sigma(\boldsymbol{x}) \simeq \sigma_{\text{RBF}}(\boldsymbol{x}) = \sum_{j=1}^{N_S}\Theta_j\Phi(\boldsymbol{x},\boldsymbol{x}_j)+\sum_{q=1}^{m}\kappa_q P_q(\boldsymbol{x}), \tag{23}$$

where $N_S = N_p + 2n_v$, and Θ_j and κ_q are the unknown interpolation coefficients computed similarly as for the ghost cells (see Appendix A.1).

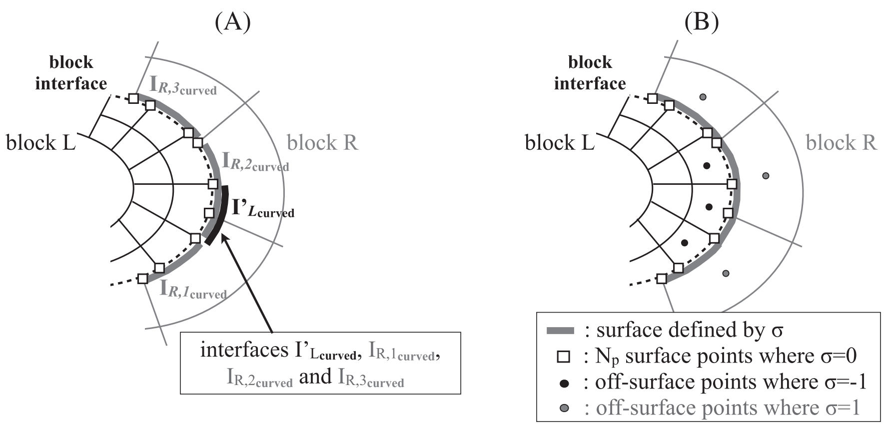

FIGURE 7 Computation of the function σ that defines the curved interfaces $I'_{L_{\text{curved}}}$ and $(I_{R,j'_{\text{curved}}})_{1\le j'\le n_v=3}$: (A) Interfaces $I'_{L_{\text{curved}}}$ and $(I_{R,j'_{\text{curved}}})_{1\le j'\le 3}$ and N_p points (squares) lying on the interfaces, and (B) surface points (squares) where $\sigma = 0$ and off-surface points (circles) where $\sigma \neq 0$

4 | PROPERTIES OF THE RBF INTERPOLATION IN THE WAVENUMBER SPACE

The performance of the RBF interpolation is evaluated in the wavenumber space. For this purpose, a uniform 1-D mesh extending over the range $[0, 1]$, composed of 81 points $(x_j)_{1\leq j\leq 81}$ is considered:

$$x_j = (j-1)\Delta \quad \text{for} \quad 1 \leq j \leq 81 \tag{24}$$

with $\Delta = 1/80$. At the points x_j, a harmonic function $f_k(x) = \exp(\mathrm{i}kx)$ is imposed, where k is the wavenumber with $k\Delta$ varying from 0 to π, and i is the complex number verifying $\mathrm{i}^2 = -1$. For RBF interpolations, a second 1-D mesh, referred to as the RBF grid, is defined using $N_{\mathrm{RBF}} = 41$ points located at the following positions:

$$x'_j = \left(0.2\Delta + \frac{j-1}{N_{\mathrm{RBF}}-1}\right) \quad \text{for} \quad 1 \leq j \leq N_{\mathrm{RBF}}. \tag{25}$$

In this way, the distance between two consecutive RBF grid points is equal to 2Δ, and there is a full point-mismatch between the two 1-D meshes. The interpolation of f_k on the RBF grid is denoted g_k in the following. For consistency with the finite-volume flux reconstruction proposed in this study, the function g_k is defined over each segment $[x'_j, x'_{j+1}]$, with $j \in [1, N_{\mathrm{RBF}}-1]$. For $x \in [x'_j, x'_{j+1}]$, from Equation (18), the function g_k writes as follows:

$$g_k(x) = \sum_{l=1}^{n_v} \xi_l \Phi(x, x_l) + P(x). \tag{26}$$

The n_v nearest mesh points (x_l) that surround point $x'_{j_{\mathrm{M}}} = (x'_j + x'_{j+1})/2$ and where the values of f_k are known are used to determine the interpolation coefficients in Equation (26). In this section, the influence of the number of points n_v is evaluated by performing interpolations using $n_v = 4$, 6, 8, and 20 points. The interpolations are carried out using the second-degree polynomial function $P(x) = \zeta_0 + \zeta_1 x + \zeta_2 x^2$, where $(\zeta_j)_{0\leq j\leq 2}$ are the unknown interpolation coefficients. The influence of the degree of P on the accuracy of the spatial discretization is discussed in Section 5.

First, the accuracy of the RBF interpolation is examined. For this purpose, an interpolation error ϵ is computed as a function of the wavenumber k from the difference between the values of f_k and g_k over each segment $[x'_j, x'_{j+1}]$ as

$$\epsilon(k) = \sum_{j=1}^{N_{\mathrm{RBF}}-1} \int_{x'_j}^{x'_{j+1}} |f_k(x) - g_k(x)| \mathrm{d}x, \tag{27}$$

where $|\cdot|$ is the complex modulus. Second, the energy of the interpolated signal g_k is compared with the energy of the original signal f_k through the evaluation of the integrals E_f and E_g defined as

$$E_f(k) = \int_{x'_1}^{x'_{N_{\mathrm{RBF}}}} |f_k(x)|^2 \mathrm{d}x = 1 \quad \text{and} \quad E_g(k) = \int_{x'_1}^{x'_{N_{\mathrm{RBF}}}} |g_k(x)|^2 \mathrm{d}x. \tag{28}$$

For comparison, interpolations are also performed using the polynomial functions of degrees 2 and 3 given by

$$P_2(x) = c_1 + c_2 x + c_3 x^2, \tag{29}$$

$$P_3(x) = c_4 + c_5 x + c_6 x^2 + c_7 x^3, \tag{30}$$

where $(c_j)_{1\leq j\leq 7}$ are the interpolation coefficients. Note that, as for the RBF interpolations, the polynomial approximations (29) and (30) are defined by pieces over each segment $[x'_j, x'_{j+1}]$. The interpolations coefficients (c_i) are determined

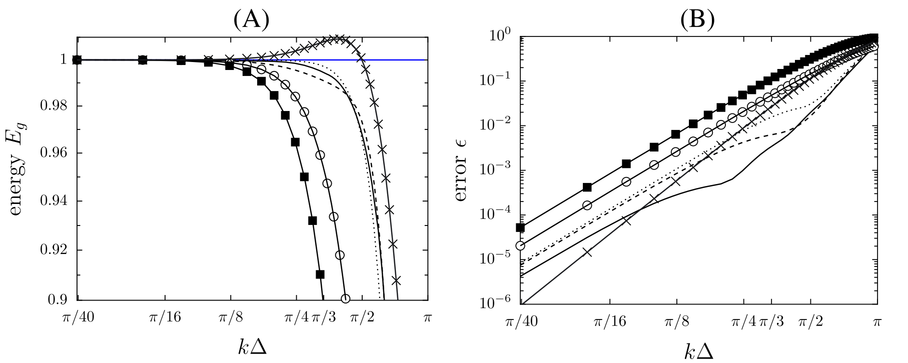

FIGURE 8 Representation of (A) the energy E_g and (B) the interpolation error ϵ as a function of the normalized wavenumber $k\Delta$: Radial basis function interpolations using ∘ $n_v = 4$, · · · · $n_v = 6$, – – – $n_v = 8$, —— $n_v = 20$, polynomial interpolations of ■ degree 2 and × degree 3. —— $E_g = E_f = 1$ [Colour figure can be viewed at wileyonlinelibrary.com]

using a least-square approximation involving n_v nearest points surrounding point x'_{j_M}. More precisely, over each segment $[x'_j, x'_{j+1}]$, the values of (c_i) are calculated to minimize the functions χ_{P_2} and χ_{P_3}:

$$\chi_{P_2}(c_1, c_2, c_3) = \sum_{l=1}^{n_v=4} \frac{|P_2(x_l) - f_k(x_l)|^2}{\left(x_l - x'_{j_M}\right)^2} \tag{31}$$

$$\chi_{P_3}(c_4, c_5, c_6, c_7) = \sum_{l=1}^{n_v=6} \frac{|P_3(x_l) - f_k(x_l)|^2}{\left(x_l - x'_{j_M}\right)^2}. \tag{32}$$

The variations of the energy E_g obtained from the RBF interpolations using $n_v = 4$, 6, 8, and 20 points and from the polynomial interpolations with P_2 and P_3 are represented in Figure 8A as a function of the normalized wavenumber $k\Delta$. When RBF is used, the value of E_g decreases with $k\Delta$, indicating higher levels of dissipation at high wavenumbers. The highest levels of dissipation are obtained using $n_v = 4$. In particular, for $k\Delta = \pi/3$, the energy is equal to 0.995 for $n_v = 4$, whereas values $0.99 < E_g < 1$ are obtained for $n_v = 6$, 8, and 20. The dissipation obtained using RBF is lower than that calculated from a polynomial interpolation of degree 2 over all the wavenumber range. In addition, using RBF, no energy amplification is observed, whereas energy values $E_g > 1$ are found using polynomial interpolation P_3 for $\pi/8 \le k\Delta \le \pi/2$ in Figure 8A. Therefore, it is interesting to use RBF to preserve the energy stability and to maintain low dissipation levels for wavenumbers $k\Delta < \pi/4$, which are well resolved by the present spatial discretization schemes.

The interpolation errors ϵ obtained using RBF and polynomial interpolations are represented in Figure 8B as a function of the wavenumber $k\Delta$. When RBF is used, the highest values of ϵ are obtained for $n_v = 4$. In this case, the interpolation error is stronger than that calculated with the polynomial interpolation P_3 for $k\Delta < \pi/2$. However, it is lower than the error computed with P_2, which involves the same number of interpolation points. When the number of interpolation points n_v increases, as expected, the value of ϵ decreases all over the wavenumber range. For $n_v = 20$, as a result, the error ϵ is lower than the error computed using P_3 for $\pi/12 < k\Delta < \pi$. For $k\Delta < \pi/12$, it is higher than that obtained using P_3, but is very small and lower than 5×10^{-6}.

5 | ACOUSTIC PULSE

To examine the overall accuracy of the flux reconstruction presented for nonconforming grids above, an acoustic pulse is imposed in the vicinity of a nonconforming interface in a medium at rest. For this purpose, the 2-D domain of size $\ell \times \ell$ shown in Figure 9A is considered, with $\ell = 100$ m. It is composed of two blocks separated by a nonconforming interface located at $x = 0.6\ell$. At $t = 0$, the pulse is introduced at $x_p = 0.4\ell$ and $y_p = 0.5\ell$ as

$$\begin{cases} \rho'(x, y) = A_p \exp\left(-\ln 2 \frac{(x-x_p)^2+(y-y_p)^2}{\hbar^2}\right) \\ u'(x, y) = v'(x, y) = 0 \\ p'(x, y) = c_0^2 \rho'(x, y), \end{cases} \tag{33}$$

where $\hbar = 0.03\ell$ is the pulse half-width, A_p is the pulse amplitude, and c_0 is the ambient sound speed. The ambient pressure and temperature are equal to $p_0 = 10^5$ Pa and $T_0 = 300$ K, respectively. Radiation boundary conditions and sponge layers are used. An exact solution of the problem can be derived from the linearized Euler equations.[10] To compare the numerical results obtained from the Navier-Stokes equations with the exact solution, an amplitude A_p of 0.1 Pa is chosen. In addition, the viscous terms in Equation (1) are neglected in the simulations.

The performance of the flux reconstruction is evaluated using six Cartesian grids referred to as pulsegrid1, pulsegrid2, pulsegrid3, pulsegrid4, pulsegrid5, and pulsegrid6, and two flux reconstruction techniques with and without RBF interpolation. The RBF interpolations are carried out using a number of $n_v = 8$ points. The influence of the degree deg(P) of the RBF polynomial function in Equation (18) is examined using polynomial functions of degrees 0, 1, and 2. For the flux reconstruction without RBF, second-order interpolations are used to reconstruct the flow variables in the ghost cells and at the grid interface.[31] This reconstruction, available in the ***elsA*** solver,[20] is described in Appendix A.3.

The mesh parameters, namely the grid spacings Δx, and the grid spacings Δy^L and Δy^R at the left-hand and right-hand sides of the block interface are given in Table 1. The meshes pulsegrid2, pulsegrid3, pulsegrid4, pulsegrid5, and pulsegrid6 are respectively 2, 3, 4, 5, and 6 times finer than pulsegrid1. In all cases, at the left-hand side of the interface, a uniform grid spacing $\Delta x = \Delta y^L$ is used in the directions x and y. For pulsegrid1, it is equal to 0.02ℓ. At the right-hand side of the interface, the grid spacing is also equal to Δx in x-direction, whereas the mesh spacing Δy^R is twice larger than Δy^L in y-direction. To have a full point-mismatch at the grid interface, for $x > 0.6\ell$, in all cases, the grid cells are shifted upwards of $0.5\Delta y^L$.

The time step Δt of the simulations is chosen sufficiently small so that the errors related to the time discretization are negligible. More precisely, its value is calculated to provide a CFL number $c_0\Delta t/\Delta x$ of 0.05 for $\Delta x = \ell/300$. The fluctuating pressure field p' obtained at $t = 1200\Delta t$ using pulsegrid2 is represented in Figure 9A. At this instant, the acoustic wave reaches the nonconforming interface. To evaluate the effective order of the spatial discretization in the presence of the nonconforming interface, the pressure fluctuation obtained at $t = 1200\Delta t$ is compared with the exact solution p'_{exact} through the L_2 relative error:

$$\epsilon_p = \left(\frac{\int_{\Omega_\epsilon} \left(p' - p'_{\text{exact}}\right)^2 \mathrm{d}\Omega}{\int_{\Omega_\epsilon} p'^2_{\text{exact}} \mathrm{d}\Omega} \right)^{1/2}, \tag{34}$$

where $\Omega_\epsilon = \{(x, y) \in \mathbb{R}^2 \,|\, 0.2\ell \le x, y \le 0.8\ell\}$. In finite volume, p' is the averaged value of the fluctuating pressure over each cell of domain Ω_ϵ (see Equation (8)). Therefore, for consistency, the exact solution is calculated similarly. The

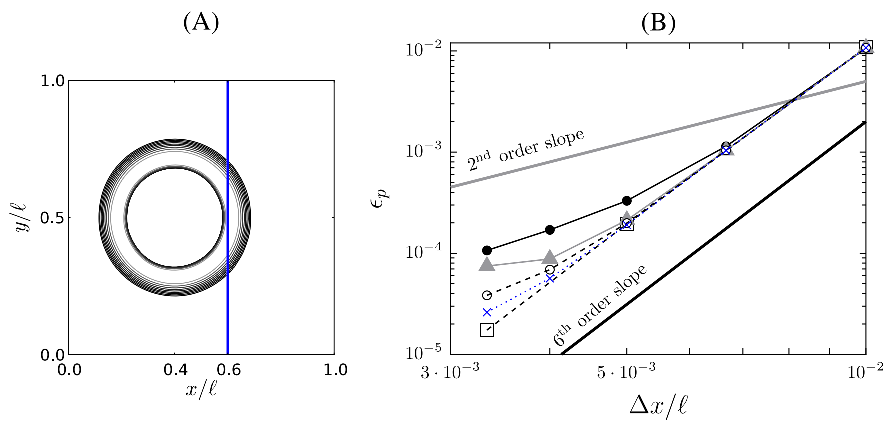

FIGURE 9 (A) Fluctuating pressure p' at $t = 1200\Delta t$ using pulsegrid2, with ten isocontours from 10^{-4} to 10^{-2} Pa following a geometric progression of ratio 1.67. The nonconforming interface is shown in blue. (B) Error profiles ϵ_p as a function of the grid spacing $\Delta x/\ell$: Radial basis function (RBF) interpolations with polynomial functions ▲ deg(P)=0, ∘ deg(P)=1, × deg(P)=2, • interpolation without RBF and □ grids without interface [Colour figure can be viewed at wileyonlinelibrary.com]

TABLE 1 Mesh spacings used in the simulations of the pulse

Mesh	Δx	Δy^L	Δy^R
pulsegrid1	$\ell/50$	$\ell/50$	$\ell/25$
pulsegrid2	$\ell/100$	$\ell/100$	$\ell/50$
pulsegrid3	$\ell/150$	$\ell/150$	$\ell/75$
pulsegrid4	$\ell/200$	$\ell/200$	$\ell/100$
pulsegrid5	$\ell/250$	$\ell/250$	$\ell/125$
pulsegrid6	$\ell/300$	$\ell/300$	$\ell/150$

discrete form of Equation (34) thus writes as

$$\epsilon_p = \left(\frac{\sum_{\text{cell} \in \Omega_e} \left(p' - p'_{\text{exact cell}}\right)^2}{\sum_{\text{cell} \in \Omega_e} p'^2_{\text{exact cell}}} \right)^{1/2}, \tag{35}$$

where $p'_{\text{exact cell}} = (1/|\Omega_{\text{cell}}|)\int_{\Omega_{\text{cell}}} p'_{\text{exact}} d\Omega$ and $|\Omega_{\text{cell}}|$ is the volume of the cell. Simulations with four uniform Cartesian meshes without grid interfaces with grid spacings of $\Delta x = \Delta y = \ell/50$, $\ell/100$, $\ell/200$ and $\ell/300$, respectively, have also been done for comparisons.

The errors ϵ_p obtained using the nonconforming grids with and without the flux reconstruction based on RBF for polynomial functions of degrees 0, 1, and 2 are presented in Figure 9B, as a function of the grid spacing $\Delta x/\ell$. Those obtained using the meshes without grid interface are also indicated. In all cases, the amplitude of ϵ_p decreases as the value of Δx tends to 0. Using the grid without interface, the error profile follows a sixth-order convergence slope. This result is expected since the present spatial discretization is based on sixth-order numerical schemes (see Pouangué et al.[12]). With nonconforming interfaces, the sixth-order convergence slope is not retrieved, and higher error levels are obtained for $\Delta x \leq 0.005\ell$ compared with the simulations without interfaces. The stronger errors are obtained using the flux reconstruction without RBF, with an error profile varying following a second-order slope. When RBF is used, lower errors are obtained, and they decrease with the degree of P. In particular, the error profile calculated with deg(P)=2 is in good agreement with that obtained for conforming grids. In the following, the RBF interpolations are therefore performed using deg(P)=2.

6 | CONVECTION OF A VORTEX

The performance of the flux reconstruction on nonconforming grids is then evaluated by performing 2-D simulations of vortex convection on Cartesian and wavy meshes.

6.1 | Cartesian grids

A round vortex is convected in a mean flow defined by a uniform Mach number M of 0.5, a pressure of 10^5 Pa and a temperature of 300 K. The 2-D computational domain used in the simulations extends from $x = 0$ down to $x = 3L$ in the streamwise direction, and from $y = 0$ up to $y = L$ in the transverse direction, where $L = 0.1$ m. It is divided into two blocks separated by a vertical nonconforming interface located at $x = L$. The vortex is defined by the velocity and pressure fluctuations:

$$\begin{cases} u' = -\frac{\Gamma}{R^2}(y - y_c) \exp\left(-\ln 2 \frac{(x-x_c)^2+(y-y_c)^2}{2b^2}\right) \\ v' = \frac{\Gamma}{R^2}(x - x_c) \exp\left(-\ln 2 \frac{(x-x_c)^2+(y-y_c)^2}{2b^2}\right) \\ p' = -\frac{\rho\Gamma^2}{2R^2} \exp\left(-\ln 2 \frac{(x-x_c)^2+(y-y_c)^2}{b^2}\right), \end{cases} \tag{36}$$

where $(x_c = 0.5L, y_c = 0.5L)$ is the position of the vortex center at the initial time $t = 0$, $b = (\sqrt{\ln 2}/20)L \simeq 0.04L$ is the vortex Gaussian half-width, and Γ represents the vortex intensity given by

$$\frac{\rho\Gamma^2}{2R^2} = 10^3 \text{ Pa}, \tag{37}$$

where $R = b/\sqrt{\ln 2}$. The velocity and pressure fluctuations are superimposed onto the mean flow at $t = 0$.

The performance of the flux reconstruction is examined by performing simulations using four meshes referred to as Finegrid, Mediumgrid, Coarsegrid, and Verycoarsegrid, and two flux reconstruction techniques with and without RBF interpolations. When RBF is applied, the influence of the number of interpolation points n_v is studied by carrying out interpolations with $n_v = 4$, 6, 8, and 12 points. The RBF interpolations are performed using a second-degree polynomial function in Equation (18). The influence of the degree of the polynomial function has been examined by performing simulations using polynomial functions of degrees 0, 1, and 2. The use of the second-degree polynomial function provided the lowest spurious noise levels at the grid interface. For the sake of concision, these results are not presented in this study. Views of the four meshes close to the block interface are given in Figure 10. The mesh parameters, including the grid spacings Δx in the streamwise direction, and the grid spacings Δy^L and Δy^R at the left-hand and right-hand sides of the block interface are provided in Table 2. In all cases, in the streamwise direction, a grid spacing of $\Delta x = \Delta = L/255$ is used. The vortex half-width b is thus discretized by ten points, given that $b = 10.6\Delta$. In the transverse direction, on the left-hand side of the interface, the grid spacing Δy^L is equal to Δ. On the right-hand side, the mesh resolution in the y-direction is different from Δ. More precisely, the grid spacing Δy^R is respectively equal to 0.5Δ, 2Δ, 4Δ, and 6Δ, for Finegrid, Mediumgrid, Coarsegrid, and Verycoarsegrid, corresponding to a discretization of the vortex half-width by 21.2, 5.3, 2.6, and 1.8 points. In addition, to ensure a full point-mismatch at the grid interface, for $x > L$, the cells are shifted upwards of $\Delta y^R/2$ for Finegrid and of $\Delta y^L/2$ for the meshes Mediumgrid, Coarsegrid, and Verycoarsegrid.

The time step Δt in the computations is chosen to impose a CFL number $(1 + M)c_0\Delta t/\Delta$ of 0.4, where c_0 is the ambient sound speed. When the vortex crosses the block interface, spurious waves are generated due to the difference in grid resolution as well as to the specific spatial discretization at the interface. The objective here is to ensure that the amplitude of these spurious waves is very low with respect to the pressure deficit in the vortex. For that, the pressure field $p_{\text{interface}}$ obtained in the multiblock simulations is compared with the pressure field $p_{\text{no-interface}}$ computed from a simulation without block interface. That monoblock simulation is carried out using the same computational domain with mesh spacings $\Delta x = \Delta y = \Delta$. By comparing the pressure $p_{\text{interface}}$ with $p_{\text{no-interface}}$ instead of with the analytical vortex solution (36), the error thus obtained only results from the effects of the nonconforming grid and not from discretization errors. In addition, the pressure field differences $\Delta p = p_{\text{interface}} - p_{\text{no-interface}}$ are only computed at the left-hand side of the block interface where the mesh is similar in the two computations. In this way, the pressure fields $p_{\text{interface}}$ and $p_{\text{no-interface}}$ are computed at the same point. In particular, the time evolution of Δp is recorded at the two mesh points A and B, indicated by squares in Figure 11. They are located, respectively, at the interface at $x = L$ and $y = 0.5L$, and upstream of the block interface at $x = 0.8L$ and $y = 0.75L$. The signal recorded at point A provides information on the vortex deformation at the block interface, while the signal at point B gives the amplitude of the spurious waves propagating from the interface.

TABLE 2 Mesh spacings for the Fine, Medium, Coarse, and Verycoarse grids

Mesh	Δx	Δy^L	Δy^R
Finegrid	Δ	Δ	$\mathbf{0.5\Delta}$
Mediumgrid	Δ	Δ	$\mathbf{2\Delta}$
Coarsegrid	Δ	Δ	$\mathbf{4\Delta}$
Verycoarsegrid	Δ	Δ	$\mathbf{6\Delta}$

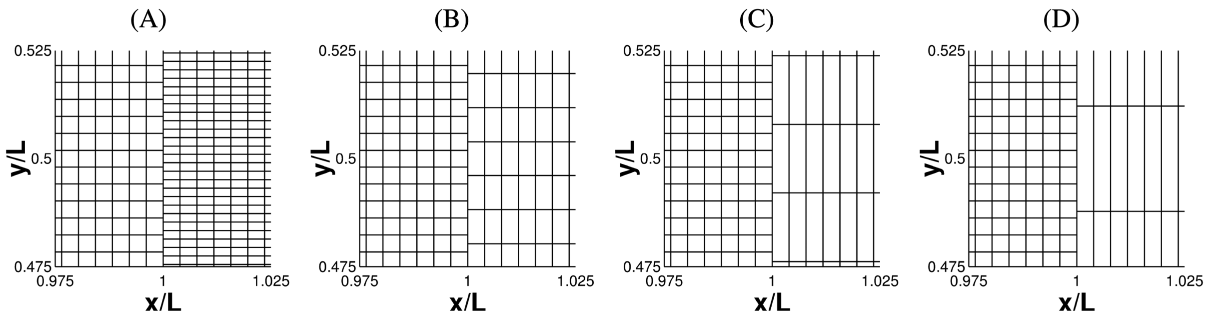

FIGURE 10 Representation of the meshes close to the block interface: (A) Finegrid, (B) Mediumgrid, (C) Coarsegrid, and (D) Verycoarsegrid

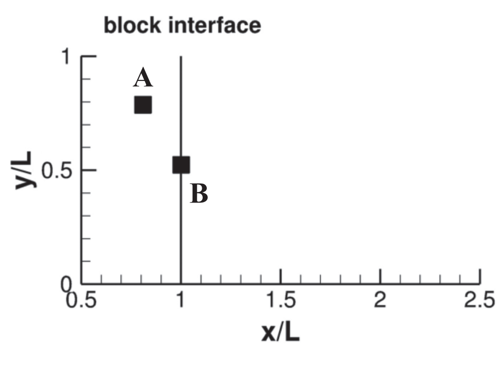

FIGURE 11 Representation of the mesh points A and B (squares) where the pressure field is recorded

Mesh	Flux reconstruction technique	n_v	RBF polynomial degree
Finegrid	RBF	8	2
Mediumgrid	RBF	8	2
Coarsegrid	RBF	8	2
Verycoarsegrid	RBF	8	2

Abbreviations: RBF, Radial basis function.

TABLE 3 Parameters of the simulations in the grid sensitivity study

6.1.1 | Grid sensitivity

The influence of the mesh resolution is evaluated by performing four simulations using Finegrid, Mediumgrid, Coarsegrid, and Verycoarsegrid. The simulation settings are given in Table 3. In the four simulations, the flux reconstruction at the block interface is performed using RBF, with interpolations on $n_v = 8$ points and the second-degree polynomial function $(P_q)_{(1,\dots,m)} = (1, x, y, x^2, y^2, xy)$.

The time evolution of the pressure $|\Delta p| = |p_{\text{interface}} - p_{\text{no-interface}}|$ recorded at points A and B in the simulations is presented in Figure 12, where $|\cdot|$ is the absolute value. The vertical blue line in the figures indicates the moment when the vortex hits the block interface. The signal amplitudes are displayed in log scale to enhance the differences between the simulations. At point A, in Figure 12A, the maximum value of $|\Delta p|$ is obtained at the instant when the vortex crosses the interface in all cases. Using Verycoarsegrid, the pressure fluctuation peak is equal to 28.1 Pa, corresponding to 2.7% of the pressure at the center of the vortex. Using Coarsegrid, the pressure difference reaches a value of 5 Pa. Using the medium and the refined meshes, the amplitudes of the spurious waves at point A are significantly lower than those found for the coarse grids, and do not exceed 0.9 Pa and 0.2 Pa, respectively. At point B in Figure 12B, the noise level also decreases as the mesh is refined at the right hand side of the block interface. Indeed, the maximum pressure differences of 3.6 Pa, 0.4 Pa, 0.1 Pa, and 0.03 Pa are obtained in Verycoarsegrid, Coarsegrid, Mediumgrid, and Finegrid. These levels are much lower than those at point A. Note that using Verycoarsegrid, the vortex half-width b is only discretized by 1.8 points at the right-hand side of the block interface. As a consequence, the mesh is not fine enough and the vortex structure is strongly modified when it crosses the block interface, yielding $|\Delta p| > 0.5$ Pa at points A and B for $t > 10000\Delta t$. These results demonstrate that nonconforming grids must be designed such that the flow field is correctly discretized at both sides of the interface. In the present simulations, given the vortex Gaussian half-width b, a grid spacing $\Delta y^R \leq 4\Delta$ is recommended, corresponding to a discretization of the half-width b by 2.6 points (ie, 5.2 points in the vortex width). This result was expected since the numerical methods used in this study well calculate the scales discretized by at least five points per wavelength.[14] Let us mention that values $\Delta y^R > 4\Delta$ could be used in sponge zones, which is to say in flow regions close to the domain boundaries where the mesh is deliberately coarse to damp hydrodynamic fluctuations before they reach the boundary conditions.

6.1.2 | Influence of the number of points used for RBF interpolations

To study the influence of the number of points n_v used for RBF interpolations, four simulations are carried out using $n_v =$ 4, 6, 8, and 12 points, respectively. The simulation parameters are given in Table 4. The medium grid with mesh spacings $\Delta x = \Delta y^L = \Delta$ and $\Delta y^R = 2\Delta$, and the second-degree polynomial function for RBF interpolation are used in all cases.

The time variations of the pressure difference $\Delta p = p_{\text{interface}} - p_{\text{no-interface}}$ recorded at points A and B are displayed in Figure 13. The maximum spurious noise levels are observed using $n_v = 4$, when interpolations are performed using four points. In this case, peaks of 1.6 Pa and 0.3 Pa are obtained at the interface and upstream. When interpolations are carried

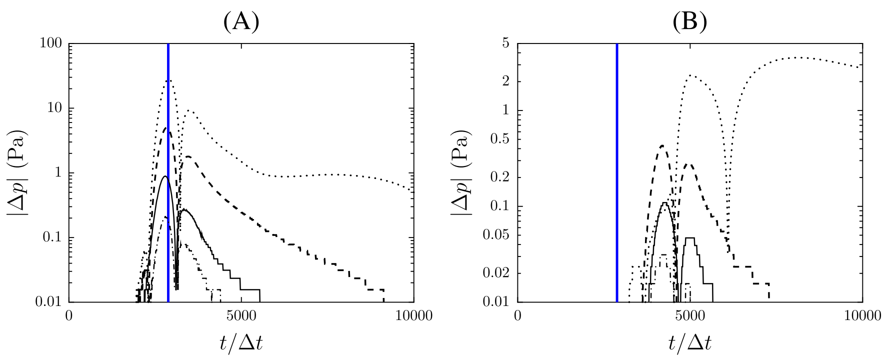

FIGURE 12 Representation of the time evolution of the pressure difference $|\Delta p| = |p_{\text{interface}} - p_{\text{no-interface}}|$ (A) at point A and (B) at point B: – · – · Finegrid, —— Mediumgrid, – – – Coarsegrid, and · · · · Verycoarsegrid. The vertical blue line indicates the moment when the vortex hits the interface [Colour figure can be viewed at wileyonlinelibrary.com]

TABLE 4 Parameters of the simulations in the study of the influence of the number of points for radial basis function (RBF) interpolations

Mesh	Flux reconstruction technique	n_v	RBF polynomial degree
Mediumgrid	RBF	**4**	2
Mediumgrid	RBF	**6**	2
Mediumgrid	RBF	**8**	2
Mediumgrid	RBF	**12**	2

out on six points, the noise levels are reduced by at least 60% at both points A and B compared to the case using $n_v = 4$. Increasing the number of interpolation points from 6 to 8 also leads to a decrease of noise levels upstream of the block interface in Figure 13B, whereas no improvement is found at the interface in Figure 13A. Finally, the pressure signals obtained using $n_v = 8$ and 12 have similar shapes suggesting that using eight points for RBF interpolations is sufficient to reach accurate results in the present test case.

6.1.3 | Influence of the flux reconstruction technique

In this section, the performance of the flux reconstruction based on RBF interpolations is compared with that of a flux reconstruction without RBF. The flux reconstruction without RBF, available in the ***elsA*** solver,[20] is described in Appendix A.3. In the following, four simulations are performed with and without RBF, using Mediumgrid and Coarsegrid. The simulation parameters are provided in Table 5. The RBF interpolations are carried out using $n_v = 8$ points and the second-degree polynomial function.

The time variations of the pressure error Δp obtained at points A and B in the simulations using Mediumgrid are presented in Figure 14. The flux reconstruction technique without RBF provides higher noise levels compared to the technique using RBF, especially at point B where the signal amplitude is 7.5 times higher. The pressure signals obtained using Coarsegrid are displayed in Figure 15. Using the RBF technique, maximum values of 5 Pa and 0.45 Pa are reached at points A and B, whereas values of 17.8 Pa and 2 Pa are obtained without RBF. Thus, the use of the flux reconstruction technique based on RBF allows us to reduce both the modifications of the vortex structure and the generation of spurious pressure waves at the block interface.

6.2 | Wavy grids

To examine the performance of the flux reconstruction for curved nonconforming interfaces, the vortex defined in Section 6.1 is convected on 2-D wavy grids. Three computational domains, presented in Figure 16, are considered. They are composed of two blocks separated by a wavy nonconforming interface located close to $x = L$, where $L = 0.1$ m. The wavy grid interfaces are defined by a sinusoidal shape of wavelength λ_x and of amplitude λ_y. The values of λ_x and λ_y are provided in Table 6 for the different meshes. In the grid referred to as wavy1, the block interface has a height of $\lambda_y = 24b$ and a sinusoidal shape of amplitude of $\lambda_x = 8b$, where b is the vortex half-width. In wavy2, the amplitude of the sinusoidal

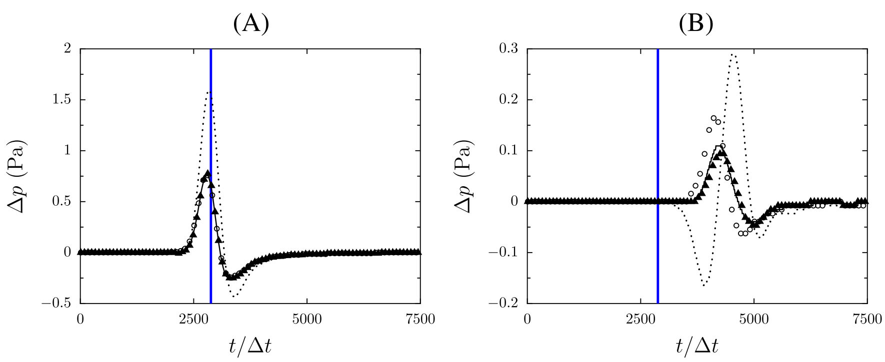

FIGURE 13 Representation of the time evolution of the pressure difference $\Delta p = p_{\text{interface}} - p_{\text{no-interface}}$ (A) at point A and (B) at point B: ···· $n_v = 4$, ∘ $n_v = 6$, ▲ $n_v = 8$ and —— $n_v = 12$ points. The vertical blue line indicates the moment when the vortex hits the interface [Colour figure can be viewed at wileyonlinelibrary.com]

TABLE 5 Parameters of the simulations in the study of the influence of the flux reconstruction technique

Mesh	Flux reconstruction technique	n_v	RBF polynomial degree
Mediumgrid	**RBF**	8	2
Mediumgrid	**no RBF**	8	2
Coarsegrid	**RBF**	8	2
Coarsegrid	**no RBF**	8	2

Abbreviation: RBF, Radial basis function.

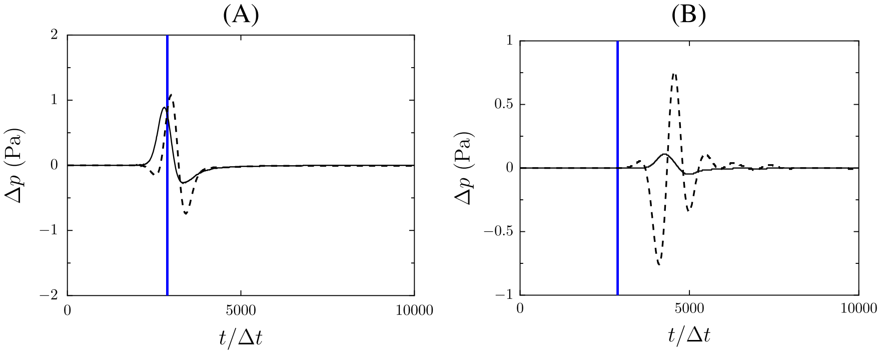

FIGURE 14 Representation of the time evolution of the pressure difference $\Delta p = p_{\text{interface}} - p_{\text{no-interface}}$ (A) at point A and (B) at point B using Mediumgrid: —— radial basis function (RBF), - - - no RBF. The vertical blue line indicates the moment when the vortex hits the interface [Colour figure can be viewed at wileyonlinelibrary.com]

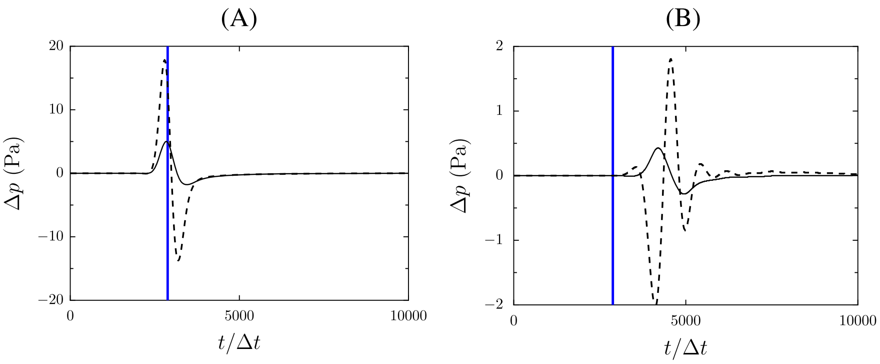

FIGURE 15 Representation of the time evolution of the pressure difference $\Delta p = p_{\text{interface}} - p_{\text{no-interface}}$ (A) at point A and (B) at point B using Coarsegrid: —— radial basis function (RBF), - - - no RBF. The vertical blue line indicates the moment when the vortex hits the interface [Colour figure can be viewed at wileyonlinelibrary.com]

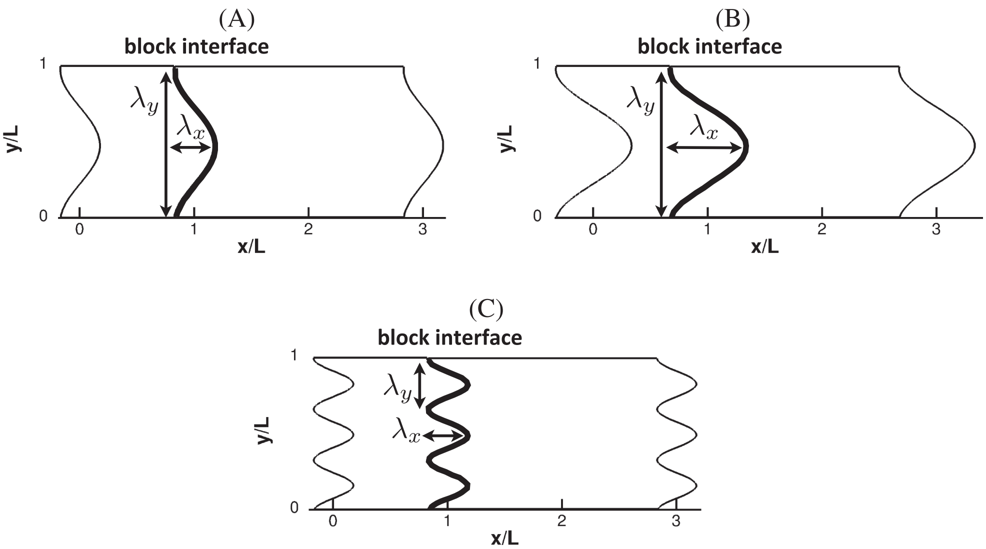

FIGURE 16 Representation of the wavy computational domains: (A) wavy1, (B) wavy2, and (C) wavy3. The nonconforming interface is indicated by a bold line

TABLE 6 Parameters of the wavy grid interfaces

Mesh	λ_x	λ_y
wavy1	$8b$	$24b$
wavy2	$16b$	$24b$
wavy3	$8b$	$8b$

interface is two times higher than in wavy1, ie, $\lambda_x = 16b$, but $\lambda_y = 24b$ as previously. In wavy3, the block interface is composed of three sinusoidal arches with $\lambda_x = \lambda_y = 8b$. In all cases, a grid spacing $\Delta x = \Delta = L/127$ is used in the x-direction, leading to a vortex half-width discretized by 5.3 points. In the y-direction, the grid spacing is equal to $\Delta y^L = \Delta$ at the left-hand side of the interface. To create nonconforming grids, a mesh spacing $\Delta y^R = L/87$ is applied at the right-hand side of the interface, yielding $b = 2.6\Delta$. The vortex, convected from the left to the right, is initially located at $y_0 = 0.5L$, and at equal distance from the domain inlet and the block interface in the x-direction.

TABLE 7 Parameters of the simulations in the study of the influence of the flux reconstruction technique for curved interfaces

Mesh	Flux reconstruction technique	n_v	RBF polynomial degree
wavy1	**RBF curve**	8	2
wavy2	**RBF curve**	8	2
wavy3	**RBF curve**	8	2
wavy1	**RBF plane**	8	2
wavy2	**RBF plane**	8	2
wavy3	**RBF plane**	8	2

Abbreviations: RBF, Radial basis function.

Six simulations are performed using wavy1, wavy2, and wavy3, and the flux reconstructions designed for plane and curved interfaces. Their parameters are given in Table 7. In all cases, RBF interpolations are carried out using a number of $n_v = 8$ points and the second-degree polynomial function. The time step Δt in the computations is chosen such that CFL number $(1 + M)c_0\Delta t/\Delta$=0.2.

The spurious noise generated at the block interface is not recorded at specific points as for the Cartesian grids in Section 6.1. Indeed, since the shapes of the block interfaces in wavy1, wavy2, and wavy3 differ, the distance between a given point and the interface is not identical in the three grids. Therefore, the computation of the pressure difference $\Delta p = p_{\text{interface}} - p_{\text{no-interface}}$ at specific points is not relevant. Instead, the pressure difference is determined over all the computational domain. To compute the pressure field $p_{\text{no-interface}}$, for each wavy grid, two simulations are carried out using conforming meshes. The first conforming mesh coincides with the nonconforming grid at the left-hand side of the interface, whereas the second mesh matches the resolution of the nonconforming grid at the right-hand side.

Snapshots of the pressure difference Δp obtained at $t = 2800\Delta t$ using wavy1 and the flux reconstruction for plane and curved interfaces are presented in Figure 17. At this time, the vortex core is located at $x = 1.5L$. In both cases, the presence of the nonconforming grid interface results in a significant discretization error around the vortex core as well as in the emission of spurious pressure waves of amplitude about 10 Pa. The simulation using the flux reconstruction technique designed for curved interfaces provides a maximum noise level of 5.2 Pa, which is two times lower than that obtained in the simulation using the reconstruction for plane interfaces.

The pressure difference Δp obtained at $t = 2800\Delta t$ using wavy2 is plotted in Figure 18. Noise levels of 10-20 Pa are found. They are higher compared with the results obtained using wavy1 in Figure 17. This is due to the block interface that displays stronger variations than that using wavy1. The pressure difference obtained in Figure 18 A with the flux reconstruction technique for curved interfaces shows weaker pressure wave amplitudes compared to the pressure difference obtained in Figure 18B for the plane interface reconstruction.

Snapshots of the pressure difference Δp obtained using wavy3 at $t = 2800\Delta t$ are displayed in Figure 19. As for wavy1 and wavy2, lower spurious noise is found using the curved reconstruction technique than the plane one. However, the use of a block interface with three arches generates higher spurious noise levels than previously, with maximum values of Δp of 200 Pa reached at this instant. In particular, the vortex core, located at $x = 1.5L$ is strongly affected by the presence of the block interface. The use of nonconforming interfaces with low curvature therefore seems to be recommended.

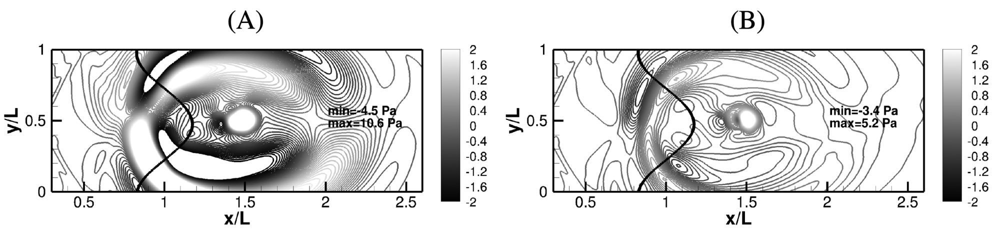

FIGURE 17 Representation of the pressure difference Δp at $t = 2800\Delta t$ using wavy1: flux reconstruction for (A) plane interfaces and (B) curved interfaces, levels given in Pa

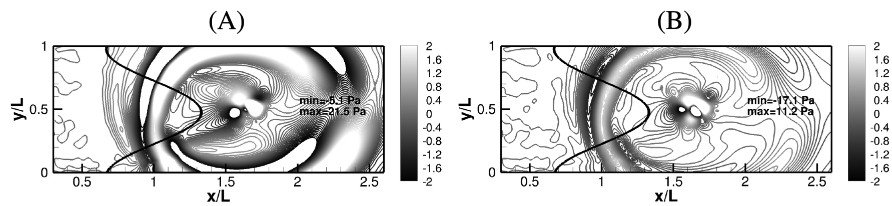

FIGURE 18 Representation of the pressure difference Δp at $t = 2800\Delta t$ using wavy2: flux reconstruction for (A) plane interfaces and (B) curved interfaces, levels given in Pa

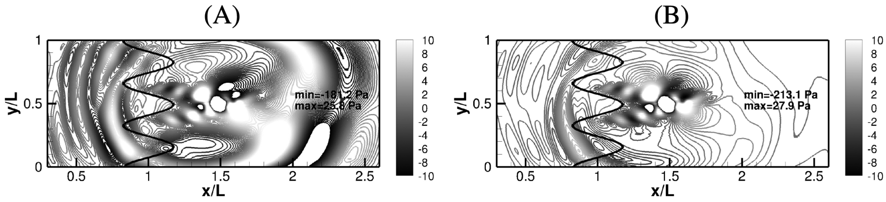

FIGURE 19 Representation of the pressure difference Δp at $t = 2800\Delta t$ using wavy3: flux reconstruction for (A) plane interfaces and (B) curved interfaces, levels given in Pa

7 | THREE-DIMENSIONAL JET

To demonstrate the applicability of the flux reconstruction technique to a 3-D simulation, a circular isothermal jet is computed using a Cartesian mesh with a nonconforming interface. The aim is to prove that the use of nonconforming interfaces does not significantly affect the jet flow development and the sound field radiated by the jet in the near-field region.

7.1 | Jet definition

The jet flow has a Mach number of $M = u_j/c_0 = 0.9$ and a Reynolds number of $Re_D = u_jD/\nu = 4 \times 10^5$, corresponding to the conditions of the jet in the numerical simulation of Bogey and Bailly,[32] where D and u_j are the jet diameter and velocity, c_0 is the sound speed and ν is the molecular viscosity. The ambient pressure p_0 and temperature T_0 are respectively equal to 10^5 Pa and 300 K. The jet inflow, located at $x = 0$, is characterized by the mean longitudinal velocity profile given by the hyperbolic tangent profile:

$$u(r) = \frac{1}{2}u_j\left(1 + \tanh\left(\frac{r_0 - r}{2\delta_\theta}\right)\right), \tag{38}$$

where $\delta_\theta = r_0/20$ is the initial momentum thickness of the shear layer, $r_0 = D/2$ is the jet radius, and $r = \sqrt{y^2 + z^2}$. The mean density profile is computed from a Crocco-Busemann relation:

$$\rho(r) = \rho_j\left(1 + \frac{\gamma - 1}{2}M^2\frac{u(r)}{u_j}\left(1 - \frac{u(r)}{u_j}\right)\right)^{-1}. \tag{39}$$

The azimuthal and radial velocities are initially null, and the pressure is equal to p_0. To seed the laminar-turbulent transition of the jet flow, vortex rings are added to the flow field in the shear layer at $x = r = r_0$, at each time step of the computation.[33] The amplitude of the perturbations is equal to $\alpha = 0.007$ and the half-width of the Gaussian profile that defines the vortices is equal to $\Delta_0 = 0.045r_0$. The small disturbances are divergence free to minimize the production of spurious acoustic waves.

7.2 | Numerical setup

Two simulations are carried out using Cartesian grids with and without a nonconforming interface. The computational domain extends from $x = 0$ up to $x = 48r_0$ in the flow direction and from 0 up to $20r_0$ in the y-direction and z-direction.

The spatial discretization in the grid without a nonconforming interface is presented in Figure 20. In the x-direction, for $0 \leq x \leq 25r_0$, the axial mesh spacing is constant with $\Delta x = 0.1r_0$, and then increases with a rate of 0.4% up to $x = 35r_0$, and with a rate of 8% for $x > 35r_0$. In the y-direction and z-direction, the mesh is finer than in the x-direction to resolve the shear layers. The grid spacing does not vary for $y, z \leq r_0$, with $\Delta y = \Delta z = r_0/30$. For $y, z > r_0$, a stretching ratio of 2% is applied up to $r = 20r_0$.

The nonconforming mesh is built from the conforming mesh. Figure 21 provides a simplified representation of the two meshes in the xy plane, with the nonconforming interface indicated by a bold line in Figure 21B. In the jet flow region, for $x \leq 14r_0$, the two meshes are identical. Downstream of the end of the jet potential core expected to be around $x_p \simeq 10r_0$ according to reference,[34] a nonconforming interface is defined at $x = 14r_0$, as shown in Figure 21B. The location of the interface is chosen downstream of the jet sound source region, which is found for $x \leq x_p$. For $x > 14r_0$, the very fine mesh spacings used in the y-direction and z-direction at the jet inlet to discretize the jet shear layers are not necessary due to the jet spreading. Therefore, downstream of the interface, the grid spacings Δy and Δz in the nonconforming mesh are twice as coarse as in the conforming grid. Thus, the number of mesh points in the nonconforming grid, equal to 42 million points, is reduced by 44% compared to the conforming grid.

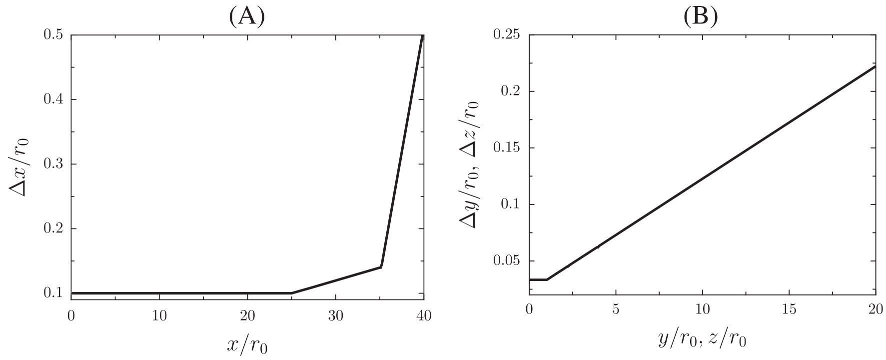

FIGURE 20 Representation of the spatial discretizations in the conforming grid: (A) axial discretization and (B) discretization in the y-direction and z-direction

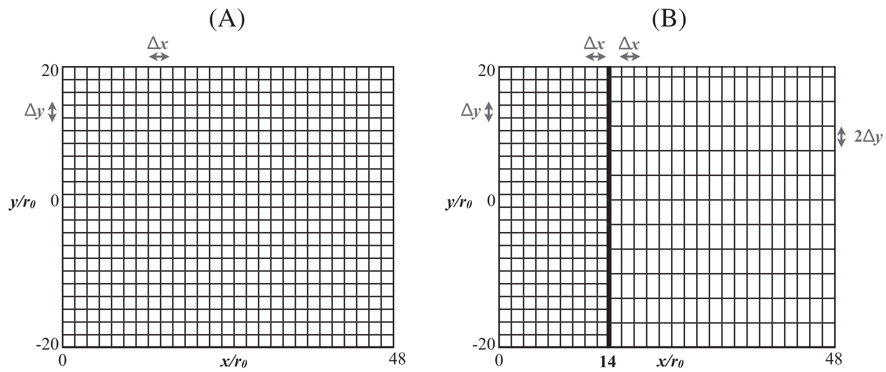

FIGURE 21 Sketch of (A) the conforming grid and (B) the nonconforming grid in the xy plane

The conforming grid used in the present work is finer than the one used by Bogey and Bailly[32] by factors of 1.3 and 2 in the axial and radial directions, respectively. In addition, since the resolutions of the two grids used in this study differ for $x > 14r_0$, small differences between the results from the two simulations are expected, as demonstrated by the grid sensitivity of turbulent jet flows presented by Bogey.[35]

In each computation, the jet flow is simulated over a time period $T = 2 \times 10^5 \Delta t = 2000 r_0/c_0$. The flow initialization lasts over $600r_0/c_0$. The velocity and pressure fields are then recorded during a sampling period $T_s = 1400r_0/c_0$, leading to a minimum Strouhal number $\mathrm{St}_{\min} = D/(T_s u_j)$ of 1.6×10^{-3}. To study the development of the jet flow, the velocity field is recorded along the jet axis and at $r = r_0$. To examine the acoustic sound radiated in the near-field region, pressure spectra at $r = 8r_0$ are computed by averaging over eight points equally distributed on circles centered on the jet axis. The data are sampled every ten time steps to compute spectra up to a maximum Strouhal number $\mathrm{St}_{\max} = fD/u_j = 5.55$, and the spectra are evaluated from overlapping samples of duration $93.3r_0/c_0$.

At the nonconforming interface, the flux reconstruction for plane interfaces presented in Section 3.1 is applied. The RBF interpolations are performed using $n_v = 8$ points and second-degree polynomial functions. The choice of the values of n_v and deg(P) is motivated by the fact that it provided accurate results for an acoustic pulse propagation and for a vortex convection on nonconforming Cartesian grids in 2-D problems (see Sections 5 and 6.1).

7.3 | Results

Snapshots of the vorticity magnitude and the fluctuating pressure obtained in the two simulations are presented in Figure 22. The nonconforming interface at $x = 14r_0$ is indicated by a vertical line in Figure 22B. In the two simulations, the jet mixing layers are found to develop from $x = r_0$ and to interact around $x = 12r_0$. Further downstream, in Figure 22B, vortical structures cross the nonconforming interface and display lower levels than those located upstream for $x < 14r_0$. These levels are also lower than those obtained for $x > 14r_0$ in Figure 22A. This is most likely due to the mesh resolution that is twice as coarse in the y-direction for $x > 14r_0$ in the nonconforming grid.[35] In the pressure field, acoustic waves propagate from the jet with an angle of about 30° relative to the x-axis. In Figure 22B, no discontinuity of the pressure waves radiated from the jet and no spurious reflection are visible in the vicinity of the nonconforming interface.

More quantitative results are shown in Figure 23, where the mean axial velocity profiles obtained in the two simulations are given along the jet axis and at $r = r_0$. In Figure 23A, the two profiles along the jet axis are superimposed for $x \leq 20r_0$. They indicate that in both jets, the jet potential core ends at $x_p = 12r_0$. For $x > 20r_0$, slightly lower velocity values are found

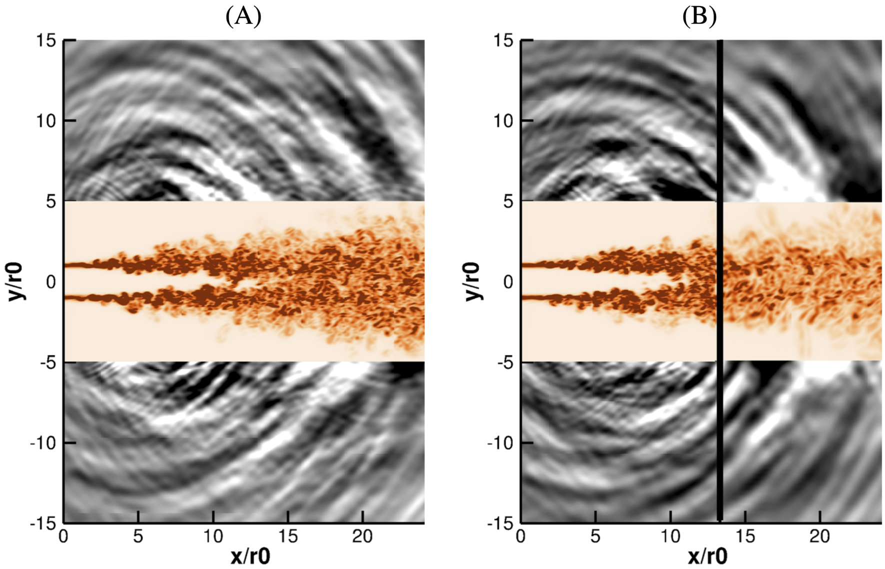

FIGURE 22 Snapshots in the *xy* plane of the vorticity modulus in the flow and of the fluctuating pressure outside obtained from the simulations using (A) a conforming grid and (B) a nonconforming grid. The color scale is from 0 to $2.5u_j/r_0$ for the vorticity and the gray scale is from -70 Pa to 70 Pa for the pressure [Colour figure can be viewed at wileyonlinelibrary.com]

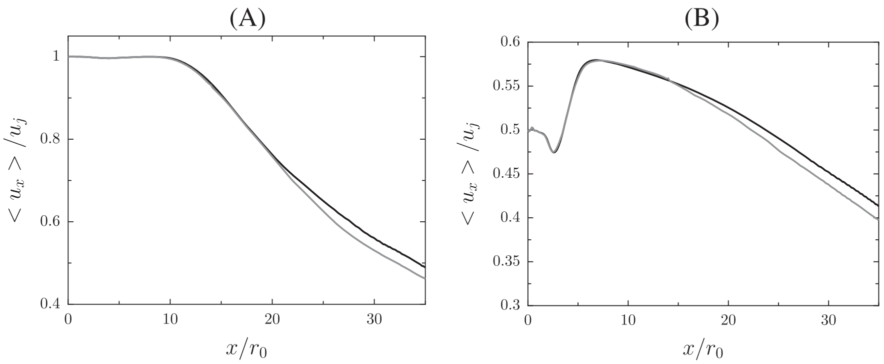

FIGURE 23 Representation of the mean axial velocity (A) along the jet centerline and (B) at $r = r_0$: simulations with —— a conforming grid and —— a nonconforming grid

using the nonconforming grid, with differences that do not exceed $0.025u_j$. In Figure 23B, the velocity profiles at $r = r_0$ are also superimposed upstream of the grid interface, whereas velocity is lower by $0.02u_j$ for $x > 14r_0$ in the simulation using a nonconforming grid.

The root-mean-square (RMS) axial and radial velocities $< u'_x u'_x >^{1/2}/u_j$ and $< u'_r u'_r >^{1/2}/u_j$ calculated at $r = r_0$ are represented in Figure 24, where the prime stands for the fluctuating quantity and $< \cdot >$ for time average. In Figures 24A and 24B, in the same way as for the mean profiles of Figure 23B, the profiles from the two simulations are identical for $x < 14r_0$, with the same peaks of turbulence. For $x \geq 14r_0$, small differences of less than 1% appear between the two computations. In particular, using a nonconforming grid, the RMS profiles slightly decrease at the nonconforming interface $x = 14r_0$ and present a small hump downstream for $17r_0 \leq x \leq 27r_0$. Despite this, for $x \geq 27r_0$, very similar turbulent levels are found in the two simulations. The small differences reported between the two simulations in Figures 23 and 24 are likely due to the resolution of the nonconforming grid that is coarser for $x \geq 14r_0$.[35]

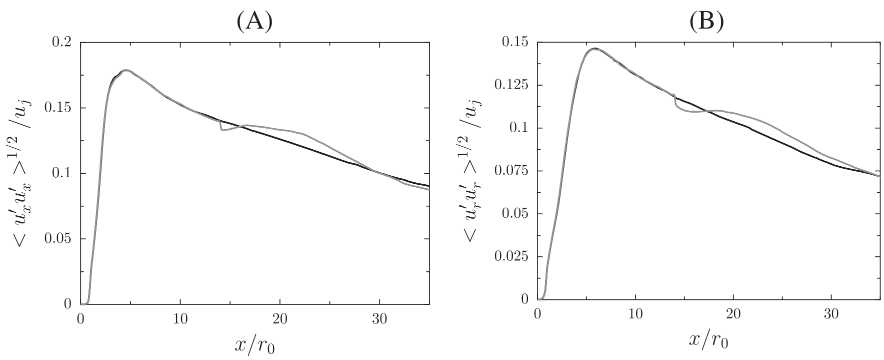

FIGURE 24 Representation of the (A) axial and (B) radial root-mean-square velocity profiles at $r = r_0$: simulations with ——a conforming grid and ——a nonconforming grid

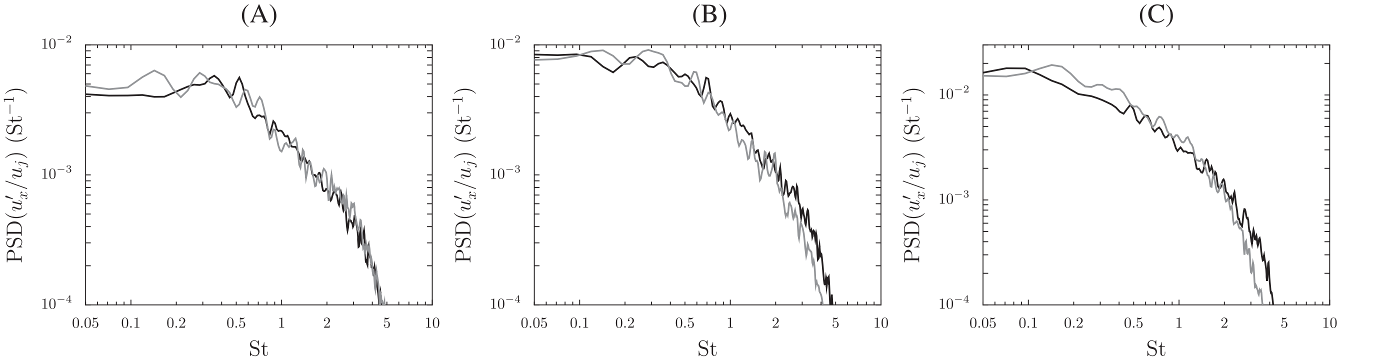

FIGURE 25 Representation of the axial velocity spectra on the jet axis (A) upstream of the grid interface at $x = 13.4r_0$, and downstream at (B) $x = 14.7r_0$ and (C) $x = 20r_0$: —— conforming grid and —— nonconforming grid

To investigate the effects of the presence of the nonconforming interface on the jet flow features, axial velocity spectra are computed at three locations along the jet axis, upstream of the nonconforming interface at $x = 13.4r_0$, and downstream of the interface at $x = 14.7r_0$ and at $x = 20r_0$. The spectra are represented in Figure 25 as a function of the Strouhal number. At $x = 13.4r_0$, the spectra exhibit similar shapes and levels, which suggests that the jet flow components are not affected by the close proximity of the nonconforming interface. Downstream of the interface, at $x = 14.7r_0$, the spectra from the two simulations show similar levels for St < 2, whereas a more pronounced decrease is observed for St ≥ 2 for the spectrum obtained using the nonconforming grid. At $x = 20r_0$, the spectrum from the nonconforming grid displays slightly higher levels at low Strouhal numbers and collapses more rapidly for St ≥ 2. The origin of the small differences observed here does not seem to be related to the presence of the nonconforming interface but to a poorer discretization of the jet coherent structures using the nonconforming mesh.[35]

Finally, to examine the acoustic results in the near-field region, pressure spectra at $r = 8r_0$ are plotted in Figure 26 for the axial positions $x = 13.4r_0$, $x = 14.7r_0$ and $x = 20r_0$. The spectra at the three locations display broadband shapes, which is typical of subsonic turbulent jet noise.[36] Upstream of the grid interface, at $x = 13.4r_0$, the spectra from the two simulations are very similar, which is expected since the two meshes are identical for $x \leq 14r_0$. Downstream of the interface, at $x = 14.7r_0$ and $x = 20r_0$, the acoustic spectra predicted by the two simulations are in good agreement for Strouhal numbers St < 2. For St ≥ 2, the spectrum obtained from the nonconforming grid collapses more rapidly. This drop is due to the lower mesh cut-off Strouhal number in that case. Indeed, at $r = 8r_0$, considering that the spatial schemes resolve wavelengths discretized by at least five points,[14] the cut-off Strouhal number is of $\mathrm{St}_{\text{cut-off}} = 2$ for the nonconforming grid and of $\mathrm{St}_{\text{cut-off}} = 4$ for the conforming grid.

These results demonstrate that the present nonconforming grid methodology can be used in order to reduce the size of the mesh and thus the computational cost, without appreciably biasing the jet development and the noise field radiated by the jet.

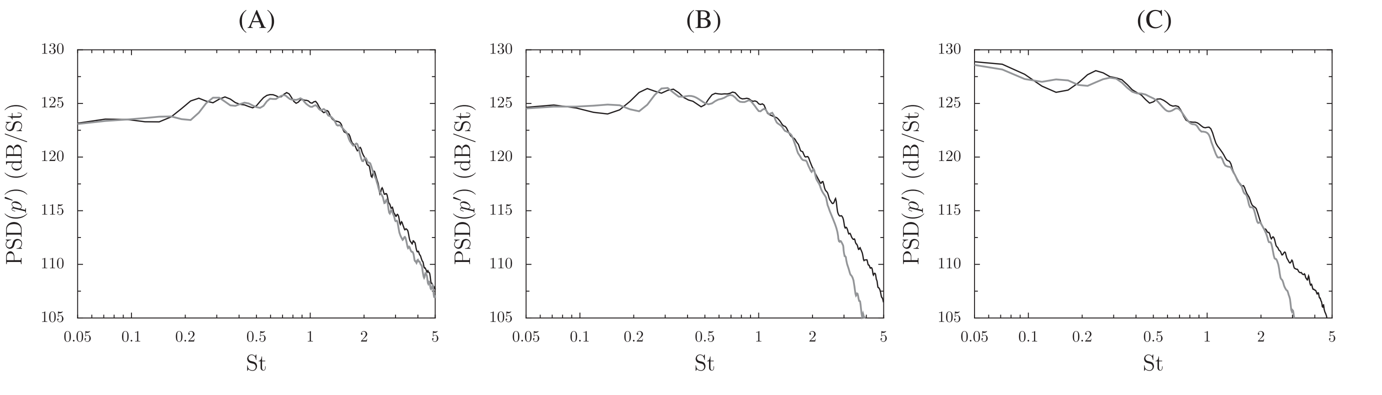

FIGURE 26 Representation of the pressure spectra at $r = 8r_0$ (A) upstream of the grid interface at $x = 13.4r_0$, and downstream at (B) $x = 14.7r_0$ and (C) $x = 20r_0$: —— conforming grid and —— nonconforming grid

8 | CONCLUSION

In this study, a flux reconstruction technique is presented to perform aeroacoustic computations using high-order finite-volume spatial schemes on structured meshes including nonconforming grid interfaces. The spatial discretization is carried out using a sixth-order implicit scheme in combination with a sixth-order implicit selective filter. The flux reconstruction can be applied to plane or curved nonconforming interfaces. It is performed using noncentered formulations for the spatial scheme and the selective filter at the nonconforming interface. These formulations require the definition of ghost cells and ghost interfaces. The flow variables in the ghost cells and at the interfaces are computed using meshless interpolations with RBFs. For computational efficiency, all the interpolation coefficients are computed once in the beginning of the simulation and then stored in memory. The properties of the RBF interpolations in the wavenumber space are studied. The accuracy of the flux reconstruction is evaluated for an acoustic pulse introduced in the vicinity of a nonconforming interface using 2-D Cartesian grids. RBF interpolations using $n_v = 8$ points in conjunction with a second-degree polynomial function are found to be sufficient to obtain accurate results. The performance of the flux reconstruction is then examined for the convection of a vortex using 2-D Cartesian and wavy grids. The results on Cartesian grids highlight the benefits of using RBF interpolations, instead of a low-order flux reconstruction, to reduce the spurious pressure waves produced at the block interface. The results obtained with different spatial resolutions also show that the nonconforming grids must be designed such that the flow field is well discretized by the mesh before and after the grid interface. The results of the computations performed on wavy grids demonstrate the advantages of using the flux reconstruction for curved interfaces. More precisely, the flux reconstruction technique designed for curved interfaces produces lower spurious noise level than those obtained using the reconstruction for plane interfaces. It seems also recommended to use low curvature nonconforming interfaces. Finally, the application of the flux reconstruction technique to 3-D flows is illustrated for a turbulent round jet flow at a diameter-based Reynolds number of 4×10^5. Simulations are performed with and without a nonconforming grid interface downstream of the jet potential core. The jet development is only slightly affected by the presence of the nonconforming grids, and the acoustic spectra in the near-field region are very similar.

ACKNOWLEDGEMENTS

This study, financially supported by Airbus, was performed at CERFACS in the context of the PhD thesis of the first author. The authors gratefully acknowledge Dr. Marc Montagnac for his crucial help in the development of the numerical code used in this work. The postprocessing of the numerical results is carried out using Antares (release 1.11.0, https://www.cerfacs.fr/antares).[37]

ORCID

Sophie Le Bras https://orcid.org/0000-0001-7859-2569

REFERENCES

1. Bailly C, Bogey C, Marsden O. Progress in direct noise computation. *Int J Aeronaut*. 2010;9(1-2):123-143.
2. Bogey C, Bailly C. A family of low dispersive and low dissipative explicit schemes for flow and noise computations. *J Comput Phys*. 2004;194(1):194-214.
3. Colonius T, Lele SK. Computational aeroacoustics: progress on nonlinear problems of sound generation. *Prog Aerosp Sci*. 2004;40(6):345-416.
4. Bogey C, Marsden O, Bailly C. Large-eddy simulation of the flow and acoustic fields of a Reynolds number 10^5 subsonic jet with tripped exit boundary layers. *Phys Fluids*. 2011;23:035104.
5. Bogey C, Bailly C. Influence of nozzle-exit boundary-layer conditions on the flow and acoustic fields of initially laminar jets. *J Fluid Mech*. 2010;663:507-538.
6. Brès GA, Jordan P, Colonius T, Le Rallic M, Jaunet V, Lele SK. Large eddy simulation of a Mach 0.9 turbulent jets. In: Proceedings of the 2014 Summer Program; 2014; Stanford, CA.
7. Desvigne D, Mardsen O, Bogey C, Bailly C. Development of noncentered wavenumber-based optimized interpolation schemes with amplification control for overlapping grids. *SIAM J Sci Comput*. 2010;32(4):2074-2098.
8. Huber J, Drochon G, Pintado-Peno A, Cléro F, Bodard G. Large-scale jet noise testing, reduction and methods validation "EXEJET": 1. project overview and focus on installation. In: 20th AIAA/CEAS Aeroacoustics Conference; 2014; Atlanta, GA.
9. Costin WJ, Allen CB. Numerical study of radial basis function interpolation for data transfer across discontinuous mesh interfaces. *Int J Numer Meth Fluids*. 2013;72(10):1076-1095.

10. Tam CKW, Webb JC. Dispersion-relation-preserving finite difference schemes for computational acoustics. *J Comput Phys*. 1993;107:262-281.
11. Lele SK. Compact finite difference schemes with spectral-like resolution. *J Comput Phys*. 1992;103:16-42.
12. Pouangué AF, Deniau H, Sicot F, Sagaut P. Curvilinear finite volume scheme using high order compact interpolation. *J Comput Phys*. 2010;229(13):5090-5122.
13. Visbal MR, Gaitonde DV. On the use of higher-order finite-difference schemes on curvilinear and deforming meshes. *J Comput Phys*. 2002;181:155-185.
14. Pouangué AF, Sanjosé M, Moreau S, Daviller G, Deniau H. Subsonic jet noise simulations using both structured and unstructured grids. *AIAA J*. 2014;53(1):55-69.
15. Biolchini R, Bailly C, Boussuge J-F, Fernando R. Numerical study on the relation between hydrodynamic fluctuations and noise in hot jets at high Reynolds numbers. In: 22nd AIAA/CEAS Aeroacoustics Conference; 2016; Lyon, France.
16. Grenson P, Deniau H. Large-eddy simulation of an impinging heated jet for a small nozzle-to-plate distance and high Reynolds number. *Int J Heat Fluid Flow*. 2017;68:348-363.
17. Arroyo CP, Daviller G, Puigt G, Airiau C, Moreau S. Identification of temporal and spatial signatures of broadband shock-associated noise. *Shock Waves*. 2018:1-18.
18. Wang JG, Liu GR. A point interpolation meshless method based on radial basis functions. *Int J Numer Methods Eng*. 2002;54(11):1623-1648.
19. Le Bras S, Deniau H, Bogey C. A flux reconstruction technique for non-conforming grid interfaces in aeroacoustic simulations. In: 22nd AIAA/CEAS Aeroacoustics Conference; 2016; Lyon, France.
20. Cambier L, Heib S, Plot S. The Onera elsA CFD software: input from research and feedback from industry. *Mech Ind*. 2013;14(03):159-174.
21. Lazareff M, Vuillot AM, Cambier L. Manuel théorique du logiciel elsA. ONERA; 2010.
22. Fauconnier D, Bogey C, Dick E. On the performance of relaxation filtering for large-eddy simulation. *J Turbul*. 2013;14(1):22-49.
23. Kremer F, Bogey C. Large-eddy simulation of turbulent channel flow using relaxation filtering: resolution requirement and Reynolds number effects. *Comput Fluids*. 2015;116:17-28.
24. Le Bras S, Deniau H, Bogey C, Daviller G. Development of compressible large-eddy simulations combining high-order schemes and wall modeling. *AIAA J*. 2017:1-12.
25. Toro EF, Spruce M, Speares W. Restoration of the contact surface in the HLL-Riemann solvers. *Shock Waves*. 1994;4(1):25-34.
26. Pouangué AF. *Schémas Volumes Finis Précis: Application à L'aéroacoustique Numérique de Jets Subsoniques* [PhD dissertation]. Paris, France: Pierre and Marie Curie University; 2011.
27. Gaitonde DV, Visbal MR. High-order schemes for Navier-Stokes equations: algorithm and implementation into FDL3DI. Fort Belvoir, VA: Defense Technical Information Center; 1998.
28. Wendland H. *Scattered Data Approximation*. Cambridge, UK: Cambridge University Press; 2004. *Cambridge Monographs on Applied and Computational Mathematics*; vol. 17.
29. Golberg MA, Chen CS, Bowman H. Some recent results and proposals for the use of radial basis functions in the BEM. *Eng Anal Bound Elem*. 1999;23(4):285-296.
30. Carr JC, Beatson RK, Cherrie JB, et al. Reconstruction and representation of 3D objects with radial basis functions. In: Proceedings of the 28th Annual Conference on Computer Graphics and Interactive Techniques; 2001; New York, NY.
31. Fillola G, Le Pape MC, Montagnac M. Numerical simulations around wing control surfaces. In: 24th International Council of Aeronautical Sciences; 2004; Yokohama, Japan.
32. Bogey C, Bailly C. Computation of a high Reynolds number jet and its radiated noise using large eddy simulation based on explicit filtering. *Comput Fluids*. 2006;35(10):1344-1358.
33. Bogey C, Bailly C, Juvé D. Noise investigation of a high subsonic, moderate Reynolds number jet using a compressible large eddy simulations. *Theor Comput Fluid Dyn*. 2003;16(4):273-297.
34. Lau JC, Morris PJ, Fisher MJ. Measurements in subsonic and supersonic free jets using a laser velocimeter. *J Fluid Mech*. 1979;93(01):1-27.
35. Bogey C. Grid sensitivity of flow field and noise of high-Reynolds-number jets computed by large-eddy simulations. *Int J Aeronaut*. 2018;17(4-5):399-424.
36. Tam CKW, Viswanathan K, Ahuja KK, Panda J. The sources of jet noise: experimental evidence. *J Fluid Mech*. 2008;615:253-292.
37. Antares Development Team. Antares Documentation Release 1.11.0. https://cerfacs.fr/antares/. Accessed 2012.

How to cite this article: Le Bras S, Deniau H, Bogey C. A technique of flux reconstruction at the interfaces of nonconforming grids for aeroacoustic simulations. *Int J Numer Meth Fluids*. 2019;91:587–614. https://doi.org/10.1002/fld.4767

APPENDIX A

CALCULATION OF RBF INTERPOLATION COEFFICIENTS

A.1 | Interpolation of the flow variables in the ghost cells

As presented in Section 3.1.3, to reconstruct the flow variables in the ghost cells, RBF interpolations are performed. An RBF interpolation u_{RBF} of the variable u at point $\boldsymbol{x}$ is defined as a linear combination of Wendland's RBFs Φ and a polynomial term:

$$u_{\mathrm{RBF}}(\boldsymbol{x}) = \sum_{j=1}^{n_v} \xi_j \Phi(\boldsymbol{x}, \boldsymbol{x}_j) + \sum_{q=1}^{m} \zeta_q P_q(\boldsymbol{x}), \tag{A1}$$

where ξ_j and ζ_q are the unknown interpolation coefficients. In this study, C^2 Wendland's basis functions[9,28] with compact support are used:

$$\Phi(\boldsymbol{x}, \boldsymbol{x}_j) = \Phi(r_j) = \left(1 - \frac{r_j}{R_v}\right)_+^4 \left(4\frac{r_j}{R_v} + 1\right) \quad \text{for } 1 \le j \le n_v \tag{A2}$$

where r_j is the Euclidian distance between the points $\boldsymbol{x}$ and $\boldsymbol{x}_j$, $\left(1 - \frac{r_j}{R_v}\right)_+$ is defined by

$$\left(1 - \frac{r_j}{R_v}\right)_+ = \begin{cases} \left(1 - \frac{r_j}{R_v}\right) & \text{if} \quad 0 \le r_j \le R_v \\ 0 & \text{if} \quad r_j > R_v \end{cases} \tag{A3}$$

and R_v is the radius of the circle of center $\boldsymbol{x}$ defined such that $R_v = Ar_{\min}$, with $r_{\min} = \min(r_j)_{(j=1,\ldots,n_v)}$ and A is a value chosen such that n_v cells are contained inside the circle. A representation of the ghost cell and the n_v cells is provided in Figure A1.

The values of ξ_j and ζ_q are determined so that the approximation $u_{\mathrm{RBF}}(\boldsymbol{x})$ is exact for all the n_v points. Therefore, the interpolation formulation (A1) satisfies the following relations:

$$u_{\mathrm{RBF}}(\boldsymbol{x}_k) = u_k = \sum_{j=1}^{n_v} \xi_j \Phi(\boldsymbol{x}_k, \boldsymbol{x}_j) + \sum_{q=1}^{m} \zeta_q P_q(\boldsymbol{x}_k) \quad \text{for} \quad 1 \le k \le n_v, \tag{A4}$$

where $(u_k)_{k=1,\ldots,n_v}$ are the values of u known in the n_v cells considered for the interpolation. To ensure that approximation (A1) has a unique solution,[18,29] the following orthogonality constraints are imposed:

$$\sum_{j=1}^{n_v} P_q(\boldsymbol{x}_j)\xi_j = 0 \quad \text{for} \quad 1 \le q \le m. \tag{A5}$$

Therefore, the values of ξ_j and ζ_q are computed by resolving the linear system:

$$\mathbf{M}\begin{pmatrix} \boldsymbol{\xi} \\ \boldsymbol{\zeta} \end{pmatrix} = \begin{pmatrix} \boldsymbol{\Phi} & \mathbf{P} \\ \mathbf{P}^T & \mathbf{0} \end{pmatrix}\begin{pmatrix} \boldsymbol{\xi} \\ \boldsymbol{\zeta} \end{pmatrix} = \begin{pmatrix} \mathbf{u}^{\mathrm{set}} \\ \mathbf{0} \end{pmatrix}, \tag{A6}$$

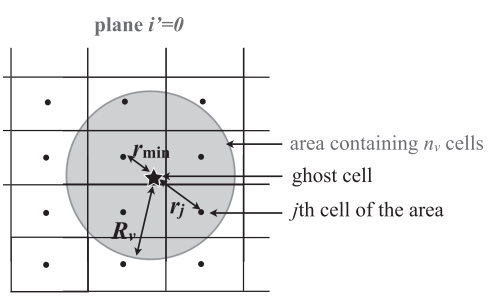

FIGURE A1 Representation of the cloud of n_v cells used for the interpolation of the flow variables in the ghost cell. The center of the ghost cell is indicated by a star where $\boldsymbol{\xi} = (\xi_1, \ldots, \xi_{n_v})^T$ and $\boldsymbol{\zeta} = (\zeta_1, \ldots, \zeta_m)^T$ are the vectors of the interpolation coefficients to be determined, $\mathbf{u}^{\text{set}} = (u_1, \ldots, u_{n_v})^T$, and $\Phi \in \mathbb{R}^{n_v \times n_v}$ and $\mathbf{P} \in \mathbb{R}^{n_v \times m}$ are the matrices defined by

$$\begin{aligned} \Phi_{kj} &= \Phi(\boldsymbol{x}_k, \boldsymbol{x}_j) \quad \text{for } 1 \leq k, j \leq n_v \\ \mathbf{P}_{kq} &= P_q(\boldsymbol{x}_k) \qquad \text{for } 1 \leq k \leq n_v \text{ and } 1 \leq q \leq m \end{aligned} \tag{A7}$$

The solution of the system (A6) writes

$$\begin{pmatrix} \boldsymbol{\xi} \\ \boldsymbol{\zeta} \end{pmatrix} = \mathbf{M}^{-1} \begin{pmatrix} \mathbf{u}^{\text{set}} \\ \mathbf{0} \end{pmatrix} = \begin{pmatrix} \sum_{k=1}^{n_v} m_{1,k} u_k \\ \vdots \\ \sum_{k=1}^{n_v} m_{n_v+m,k} u_k, \end{pmatrix} \tag{A8}$$

where $m_{i,j}$ are the coefficients of the matrix $\mathbf{M}^{-1}$. Introducing Equation (A8) in Equation (A1), the RBF interpolation applied to a ghost cell of center $\boldsymbol{x}_{\text{ghost}}$ is given by the relation:

$$u_{\text{RBF}}(\boldsymbol{x}_{\text{ghost}}) = \sum_{k=1}^{n_v} \Psi_k(\boldsymbol{x}_{\text{ghost}}) u_k, \tag{A9}$$

where the coefficients $\Psi_k(\boldsymbol{x}_{\text{ghost}})$ are defined as

$$\Psi_k(\boldsymbol{x}_{\text{ghost}}) = \sum_{j=1}^{n_v} m_{j,k} \Phi(\boldsymbol{x}_{\text{ghost}}, \boldsymbol{x}_j) + \sum_{q=1}^{m} m_{n_v+q,k} P_q(\boldsymbol{x}_{\text{ghost}}). \tag{A10}$$

Note that the n_v coefficients $\Psi_k(\boldsymbol{x}_{\text{ghost}})$ are independent of the flow variables. Therefore, they are computed and stored in memory at the beginning of the simulation. The interpolation is therefore performed at a low CPU cost since the value of u_{RBF} is simply obtained from the sum (A9).

A.2 | Interpolation of the flow variables at the nonconforming grid interface

A.2.1 | Plane interfaces

As described in Section 3.1.3, the interpolation formulation at the block interface writes

$$\begin{aligned} \tilde{u}_{L'} &= \frac{1}{|I'_L|} \int_{I'_L} u_{\text{RBF}}(\boldsymbol{x}) \text{d}\boldsymbol{x} \\ &= \sum_{j'=1}^{n_v} \widetilde{\xi}_{j'} \left(\frac{1}{|I'_L|} \int_{I'_L} \Phi(\boldsymbol{x}, \boldsymbol{x}_{j'}) \text{d}\boldsymbol{x} \right) + \sum_{q=1}^{m} \widetilde{\zeta}_q \left(\frac{1}{|I'_L|} \int_{I'_L} P_q(\boldsymbol{x}) \text{d}\boldsymbol{x} \right) \end{aligned} \tag{A11}$$

The interpolation coefficients $\widetilde{\xi}_{j'}$ and $\widetilde{\zeta}_q$ are determined by integrating Equation (A1) on the n_v interfaces $(I_{R,1}, \ldots, I_{R,j'}, I_{R,j'+1}, \ldots, I_{R,n_v})$ of Figure 5C, and by imposing that the integrals obtained are equal to the component $\tilde{u}$ of vectors $(\widetilde{\mathbf{U}}_{R,1}, \ldots, \widetilde{\mathbf{U}}_{R,j'}, \ldots, \widetilde{\mathbf{U}}_{R,n_v})$ of block R. It yields for the interface $I_{R,k}$:

$$\tilde{u}_{R,k} = \sum_{j'=1}^{n_v} \widetilde{\xi}_{j'} \left(\frac{1}{|I_{R,k}|} \int_{I_{R,k}} \Phi(\boldsymbol{x}, \boldsymbol{x}_{j'}) \text{d}\boldsymbol{x} \right) + \sum_{q=1}^{m} \widetilde{\beta}_q \left(\frac{1}{|I_{R,k}|} \int_{I_{R,k}} P_q(\boldsymbol{x}) \text{d}\boldsymbol{x} \right) \quad \text{for } 1 \leq k \leq n_v, \tag{A12}$$

where $\tilde{u}_{R,k}$ is a component of the averaged field $\widetilde{\mathbf{U}}_{R,k}$ at the interface $I_{R,k}$. In practice, the coefficients $\widetilde{\xi}_{j'}$ and $\widetilde{\zeta}_q$ are estimated by solving the linear system:

$$\begin{pmatrix} \tilde{\Phi} & \widetilde{\mathbf{P}} \\ \widetilde{\mathbf{P}}^T & \mathbf{0} \end{pmatrix} \begin{pmatrix} \widetilde{\boldsymbol{\xi}} \\ \widetilde{\boldsymbol{\zeta}} \end{pmatrix} = \begin{pmatrix} \tilde{\mathbf{u}}^{\text{set}} \\ \mathbf{0} \end{pmatrix}, \tag{A13}$$

where $\widetilde{\boldsymbol{\xi}} = (\widetilde{\xi}_1, \ldots, \widetilde{\xi}_{n_v})^T$ and $\widetilde{\boldsymbol{\zeta}} = (\widetilde{\zeta}_1, \ldots, \widetilde{\zeta}_m)^T$ are the vectors of the interpolation coefficients, $\tilde{\mathbf{u}}^{\text{set}} = (\tilde{u}_{R,1}, \ldots, \tilde{u}_{R,n_v})^T$, and $\widetilde{\boldsymbol{\Phi}} \in \mathbb{R}^{n_v \times n_v}$ and $\widetilde{\mathbf{P}} \in \mathbb{R}^{n_v \times m}$ are the matrices defined by

$$\widetilde{\boldsymbol{\Phi}}_{kj'} = \frac{1}{|I_{R,k}|} \int_{I_{R,k}} \Phi(\boldsymbol{x}, \boldsymbol{x}_{j'}) \mathrm{d}\boldsymbol{x} \quad \text{for } 1 \le k, l \le n_v \tag{A14}$$

$$\widetilde{\mathbf{P}}_{kq} = \frac{1}{|I_{R,k}|} \int_{I_{R,k}} P_q(\boldsymbol{x}) \mathrm{d}\boldsymbol{x} \qquad \text{for } 1 \le k \le n_v \text{ and } 1 \le q \le m$$

As in Section A.1, the RBF interpolation (A11) can be reformulated as

$$\tilde{u}_{L'} = \sum_{k=1}^{n_v} \widetilde{\Psi}_k u_k, \tag{A15}$$

where the coefficients $\widetilde{\Psi}_k$ are defined as

$$\widetilde{\Psi}_k = \sum_{j'=1}^{n_v} \frac{1}{|I'_L|} \int_{I'_L} m'_{j',k} \Phi(\boldsymbol{x}, \boldsymbol{x}_{j'}) \mathrm{d}\boldsymbol{x} + \sum_{q=1}^{m} m'_{n_v+q,k} \frac{1}{|I'_L|} \int_{I'_L} P_q(\boldsymbol{x}) \mathrm{d}\boldsymbol{x}, \tag{A16}$$

where $m'_{i,j}$ are the coefficients of the inverse of the matrix of the system (A13). In practice, the values of $\widetilde{\Psi}_k$ are computed only once and then stored in memory at the beginning of the simulation.

A.2.2 | Curved interfaces

To take into account the curvature effect of grid interfaces, the interface $I'_{L_{\text{curved}}}$ is defined by the function σ. The interpolation formulation to compute the flow component u at the interface $I'_{L_{\text{curved}}}$ writes, as in Equation (A11):

$$\begin{aligned} \tilde{u}_{L'} &= \frac{1}{\left|I'_{L_{\text{curved}}}\right|} \int_{I'_{L_{\text{curved}}}} u_{\text{RBF}}(\boldsymbol{x}) \mathrm{d}\boldsymbol{x} \\ &= \sum_{j'=1}^{n_v} \widetilde{\xi}_{j'} \left(\frac{1}{\left|I'_{L_{\text{curved}}}\right|} \int_{I'_{L_{\text{curved}}}} \Phi(\boldsymbol{x}, \boldsymbol{x}_{j'}) \mathrm{d}\boldsymbol{x} \right) + \sum_{q=1}^{m} \widetilde{\zeta}_q \left(\frac{1}{\left|I'_{L_{\text{curved}}}\right|} \int_{I'_{L_{\text{curved}}}} P_q(\boldsymbol{x}) \mathrm{d}\boldsymbol{x} \right) \end{aligned} \tag{A17}$$

The interpolation coefficients $\widetilde{\xi}_{j'}$ and $\widetilde{\zeta}_q$ are calculated by integrating Equation (A1) on the n_v interfaces $(I_{R,1_{\text{curved}}}, \ldots, I_{R,j'_{\text{curved}}}, I_{R,j'+1_{\text{curved}}}, \ldots, I_{R,n_{v\text{curved}}})$ also defined by the function σ, and by imposing that the integrals thus obtained are equal to the component $\tilde{u}$ of vectors $(\widetilde{\mathbf{U}}_{R,1}, \ldots, \widetilde{\mathbf{U}}_{R,j'}, \ldots, \widetilde{\mathbf{U}}_{R,n_v})$ of block R. It yields for the interface $I_{R,k_{\text{curved}}}$:

$$\tilde{u}_{R,k} = \sum_{j'=1}^{n_v} \widetilde{\xi}_{j'} \left(\frac{1}{\left|I_{R,k_{\text{curved}}}\right|} \int_{I_{R,k_{\text{curved}}}} \Phi(\boldsymbol{x}, \boldsymbol{x}_{j'}) \mathrm{d}\boldsymbol{x} \right) + \sum_{q=1}^{m} \widetilde{\zeta}_q \left(\frac{1}{\left|I_{R,k_{\text{curved}}}\right|} \int_{I_{R,k_{\text{curved}}}} P_q(\boldsymbol{x}) \mathrm{d}\boldsymbol{x} \right) \qquad \text{for } 1 \le k \le n_v, \tag{A18}$$

where $\tilde{u}_{R,k}$ is a component of the averaged field $\widetilde{\mathbf{U}}_{R,k}$ at the interface $I_{R,k_{\text{curved}}}$. The coefficients $\widetilde{\xi}_{j'}$ and $\widetilde{\zeta}_q$ are then computed from the resolution of a linear system similar to (A13).

A.3 | Flux reconstruction without RBF interpolation

The technique of flux reconstruction without RBF interpolation is identical to the technique presented in Section 3, except for the calculation of the flow variables in the ghost cells and at the grid interfaces which is performed using 2nd-order interpolations.

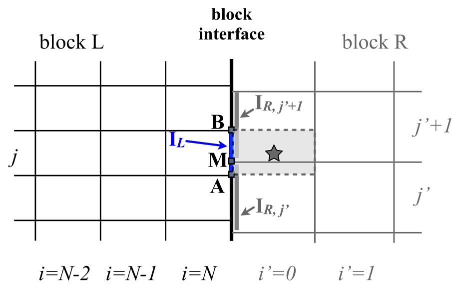

FIGURE A2 Representation of a nonconforming grid where the interface I_L is divided in two interfaces I_{AM} and I_{MB}. The flow variables in the ghost cell indicated in gray are computed as a weighted sum of the flow variables in cells $(i' = 0, j')$ and $(i' = 0, j' + 1)$ [Colour figure can be viewed at wileyonlinelibrary.com]

A.3.1 | Interpolation for ghost cells

The interpolation technique is described for the calculation of the flow variables $\mathbf{U}$ in the ghost cell located at $(i' = 0, j)$ in Figure 5A. For this purpose, as shown in Figure A2, the interface I_L in blue is divided in two parts I_{AM} and I_{MB}. The interface I_{AM} is the intersection between the interfaces I_L and $I_{R,j'}$, and the interface I_{MB} is the intersection between the interfaces I_L and $I_{R,j'+1}$. The value of $\mathbf{U}$ in the ghost cell is determined as the weighted sum of $\mathbf{U}$ in the cells $(i' = 0, j')$ and $(i' = 0, j' + 1)$ in block R:

$$\mathbf{U}_{i'=0,j} = \frac{S_{\mathrm{AM}}}{S_{\mathrm{AB}}}\mathbf{U}_{i'=0,j'} + \frac{S_{\mathrm{BM}}}{S_{\mathrm{AB}}}\mathbf{U}_{i'=0,j'+1}, \tag{A19}$$

where S_k is the surface of interface I_k. Similarly, the value of $\mathbf{U}$ in the second ghost cell in Figure 5A is calculated as the weighted sum of $\mathbf{U}$ in the cells $(i' = 1, j')$ and $(i' = 1, j' + 1)$.

A.3.2 | Interpolation at the grid interface

In order to compute the convective flux at the nonconforming interface, the value of the vector $\widetilde{\mathbf{U}}$ at the ghost interface I'_L in block R is computed as the weighted sum:

$$\widetilde{\mathbf{U}}'_L = \frac{S_{\mathrm{AM}}}{S_{\mathrm{AB}}}\widetilde{\mathbf{U}}_{R,j'} + \frac{S_{\mathrm{BM}}}{S_{\mathrm{AB}}}\widetilde{\mathbf{U}}_{R,j'+1}, \tag{A20}$$

where the values of $\widetilde{\mathbf{U}}$ at the interfaces $I_{R,j'}$ and $I_{R,j'+1}$ are computed from the upwind scheme (14). The value of $\widetilde{\mathbf{U}}$ at the interface I_L is calculated from the upwind scheme (13). Finally, the convective flux at the block interface is determined from the values of $\widetilde{\mathbf{U}}_L$ and $\widetilde{\mathbf{U}}'_L$ by resolving a Riemann flux problem.[25]